



POLITECNICO

MILANO 1863

Department of Aerospace Science and Technology
Space Propulsion
A.Y. 2023/2024

Professor: Filippo Maggi

Preliminary sizing of a bipropellant blowdown pressurized LRE

Team
NASA: Not A Space Assignment

Name	Person Code	Email
Yijing Huang	10764920	yijing.huang@mail.polimi.it
Cristian Mandolini	10724204	cristian.mandolini@mail.polimi.it
Maurizio Ondeggia	10731667	maurizio.ondeggia@mail.polimi.it
Adam Lakrad	10727361	adam.lakrad@mail.polimi.it
Francesco Gardiol	10727581	francesco.gardiol@mail.polimi.it
Chiara Conte	10703587	chiara.conte@mail.polimi.it
Elisa Fiume	10719352	elisa.fiume@mail.polimi.it
Martina Angela Vurro	11009775	martinaangela.vurro@mail.polimi.it
Emanuele Gallo	10766758	emanuele.gallo@mail.polimi.it

Date: 16/04/2024

Contents

1	Introduction	1
1.1	Requirements	1
2	Literature review	1
2.1	Nozzle losses	1
2.1.1	2D losses	1
2.1.2	Nozzle geometry	1
2.2	Blowdown architecture	2
2.3	Propellant overview	2
2.4	Material overview	3
2.4.1	Engine Material	3
2.4.2	Thermal Barrier Coating	3
2.4.3	Tank Material	4
2.5	Metallic additive manufacturing uncertainty	4
3	Modelling approach	5
3.1	Combustion and CEAM	5
3.2	Sizing	6
3.2.1	Performance	6
3.2.2	Nozzle	7
3.2.3	Combustion Chamber	8
3.2.4	Injector design	8
3.2.5	Feeding Architecture and Pressure Drop	10
3.2.6	Blowdown ratio and Propellant quantity estimation	11
3.2.7	Tank Sizing	12
3.2.8	Sizing results	13
3.3	Blowdown cycle	14
3.4	Engine cooling	17
3.4.1	Radiative cooling	18
3.4.2	Cooling Jacket with RP-1	18
3.4.3	Alternative solution	19
3.5	Additive manufacturing variations	19
3.6	Shapiro's equations	20
4	Results and comments	20
4.1	Nominal case	20
4.2	Additive manufacturing	23
4.3	Shapiro's equations results	24
5	Conclusion	25
References		
Appendix A		
Appendix B		
Declaration of Authorship		

List of Figures

1	Schematic diagram of a typical bipropellant blowdown pressurized gas feed system with two thrusters. [41]	2
2	Positive expulsion Devices to Manage Propellant [20]	2
3	Comparison of Metallic Additive Manufacturing Processes [15]	5
4	Rao nozzle with 80% length	7
5	Qualitative representation of the feeding line architecture.	10
6	Qualitative pressure cascade [20]	11
7	Qualitative 3D render of the complete system.	14
8	Visual representation of time and space computational separation	14
9	Equivalent electric circuit of the heat transfer model	19
10	Dependency of the t_{YSZ} on the ΔT	19
11	Variation of thrust, specific impulse, O/F with oxidizer (blue) and fuel (red), P_c , \dot{m} , and c^* versus time.	21
12	Variation of helium pressure in oxidizer (blue) and fuel (red) tanks, total expelled mass for both oxidizer and fuel, helium temperature for both tanks, percentage of pressure loss, and trust coefficient versus time.	22
13	Variation of Mach number at throat, in combustion chamber, P_e and v_e versus time.	23
14	Variation due to AM. Blue: nominal case, red: lower bound of accuracy, yellow: upper bound of accuracy, dashed: variation due to C_D .	23
15	Combustion gases entropy (on the left), static temperature (at the center) and Mach number (on the right) along the divergent at different time steps	24
16	Influence Coefficients for Variables Specific Heat and Molecular Weight	24
17	Static and total pressure plots along the divergent for different time instants	24
18	Static and total temperature plots along the divergent for different time instants	24
19	Combustion gases specific heat and entropy plots along the divergent for different time instants	24
20	Exit velocity and combustion gases density plots along the divergent for different time instants	24
21	Mach and sonic velocities plots along the divergent for different time instants	24
22	Alternative design of combustion chamber, fixing $M_c = 0.2$	24
23	Rao nozzle [41]	24
24	Initial and final parabola angles for Rao nozzle [41].	24
25	Vacuum Specific Impulse Versus Mixture Ratio for LOX and RP-1 Computed for 50 bar of Chamber Pressure	24
26	Type of injector chosen [41]	24
27	residence time during the mission	24

List of Tables

1	Nominal requirements	1
2	Examples of LOX/RP-1 thrust values	3
3	Properties of propellant	3
4	Additive manufacturing uncertainties in best, worst and average case scenario	5
5	Length and 2D losses coefficient for 15° conical nozzle and both 80% and 100% length Rao nozzle	8
6	Values for the injection plate	8
7	Atomization input data	9
8	Atomization output data	9
9	Parameters of the LOX and RP-1 tanks.	13
10	Helium mass and density for 90 K and 273.15 K storage.	13
11	Initial mass, volume, temperature and pressure of LOX, RP1, and He of both tanks	13
12	Dimensions of the whole system.	13
13	Cooling input	18

14	Radiative cooling	18
15	Initial and final values for relevant quantities	20

Nomenclature

C_D	Discharge Coefficient	M_m	Molecular Mass
SMD	Sauter Mean Diameter	P_c	Chamber Pressure
TBC	Thermal Barrier Coating	P_e	Static Pressure at nozzle exit
α	Divergent Semi Aperture Angle	P_{He}	Helium pressure
β	Convergent Semi Aperture Angle	P_t	Tank Pressure
ΔP_{conc}	Concentrated pressure losses	P_t	Tank Pressure
ΔP_{dis}	Distributed pressure losses	T_f	Combustion flame temperature
ΔP_{feed}	Feeding line pressure losses	u_e	velocity at nozzle exit
ΔP_{inj}	Injectors pressure losses	u_p	Pipes Velocity
\dot{m}_p	Mass flow rate	AM	Additive Manufacturing
ε	Expansion Ratio	APS	Atmospheric Plasma Spray
ε_c	Contraction Ratio	$CEAM$	Chemical Equilibrium with Applications for Matlab
γ	Specific Heat ratio	DED	Directed Energy Deposition
λ	Correction Factor	O/F	Oxidizer to Fuel Ratio
A_e	Exit area	PBF	Powder-Bed Fusion
A_t	Throat area	SLM	Selective Laser Melting
B	Blowdown ratio	T_{wc}	Cold wall temperature
c_p	Specific Heat at constant Pressure	T_{wh}	Hot wall temperature
c_T	Thrust Coefficient	TBC	Termal Barrier Coating
I_{sp}	Specific Impulse	YSZ	Yttria-Stabilized Zirconia
L^*	Characteristic length	CFD	Computational Fluid Dynamics
M_C	Combustion chamber Mach		

1 Introduction

This report illustrates the preliminary sizing of a blowdown pressurized propulsion system based on liquid semi-cryogenic propellant (*LOX/RP-1*) to be operated in vacuum. This has to guarantee some requirements, regarding both geometry and performances, which will be detailed in Section 1.1. Initially, an examination of the nominal configuration is conducted, focusing on the assessment of thrust and specific impulse profiles, as well as computation of the total impulse, considering 2D losses. Secondly, the possibility of cooling the engine with RP-1 is checked and commented. After that, an analysis is performed to investigate the impact of uncertainties arising from additive manufacturing techniques on system performances comparing it to the nominal condition. Finally, Shapiro's equations are solved to determine the variation of flow properties in the nozzle divergent.

1.1 Requirements

To conduct the preliminary sizing process, a set of requirements was identified and listed in Table 1

ID	Requirement
REQ-01	The system shall use LOX/RP-1 as propellant combination.
REQ-02	The system shall operate in vacuum providing a thrust initially equal to 1000 N.
REQ-03	The initial value of the chamber pressure shall be 50 bar and the minimum of 20 bar.
REQ-04	Total space allocated to the propulsion system shall be of 2 meter length and 1 meter of diameter. The empty space shall be at least 20% of the available one.
REQ-05	The system shall be blowdown pressurized.
REQ-06	The combustion chamber and the injection plate production shall be based on additive manufacturing.

Table 1: Nominal requirements

2 Literature review

In this section a preliminary literature review is conducted before starting with the system modelling.

2.1 Nozzle losses

2.1.1 2D losses

2D losses are caused by the need of a divergence in order to expand the gasses, which causes the flow to have both an axial and a radial component. The first one contributes to thrust since it is aligned to the axis of the model. The radial component is instead orthogonal to the thrust direction, meaning that it will not contribute to it. This effect can be modelled through the correction factor λ , which adjusts the dynamic contribution of the ideal 1D thrust [20].

2.1.2 Nozzle geometry

Although a simple conical nozzle is cheap and relatively easy to fabricate, it is not the most efficient in terms of thrust losses, due to the formation of small oblique shocks when the flow expands from the throat to the exit and also because of the presence of a radial velocity component in the nozzle plane exit. It is possible to increase the performance by utilizing a bell-shaped nozzle, thanks to its wall contour, which is designed to

minimize losses. In these types of nozzles the high relative pressure, the large pressure gradient and the rapid expansion of the working fluid do not allow separation, making it possible to have a high expansion section right behind the nozzle throat, where oblique expansion waves change the flow direction with essentially no loss of energy. This is then followed by a gradual reduction of the nozzle contour slope which causes the flow to turn in the opposite direction, generating oblique compression waves where the flow is turned and velocity is slightly reduced. It is possible to balance oblique compression waves with the oblique expansion waves thanks to the nozzle contour, minimizing the energy loss. The length of these types of nozzles is usually expressed as a fraction of a reference conical nozzle with a 15° semi aperture angle and with same expansion ratio. During the 60's, G. V. R. Rao [41] developed an approach based on the fact that a parabola represents a good approximation for the bell-shaped contour curve, as shown in Figure 23. His method allows for the development of a parabolic nozzle whose length can be arbitrarily decided. It is then possible to correlate the chosen length with the correction factor so to evaluate the trade-off between 2D losses and nozzle length.

2.2 Blowdown architecture

The system uses a blowdown architecture for tank pressurization as stated by **REQ-05**. A scheme of the system is shown in Figure 1.

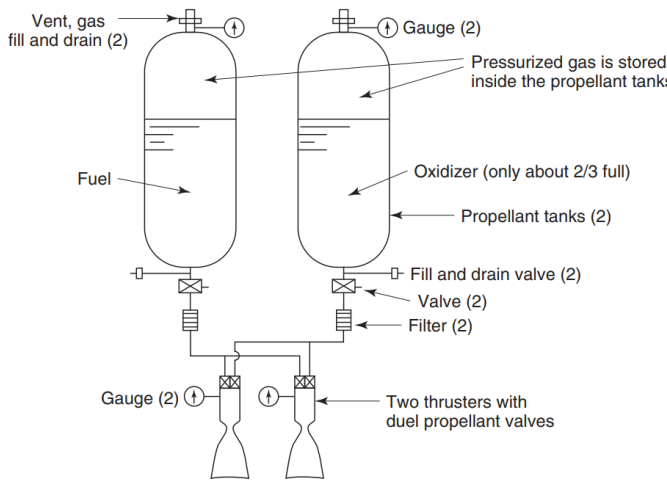


Figure 1: Schematic diagram of a typical bipropellant blowdown pressurized gas feed system with two thrusters. [41]

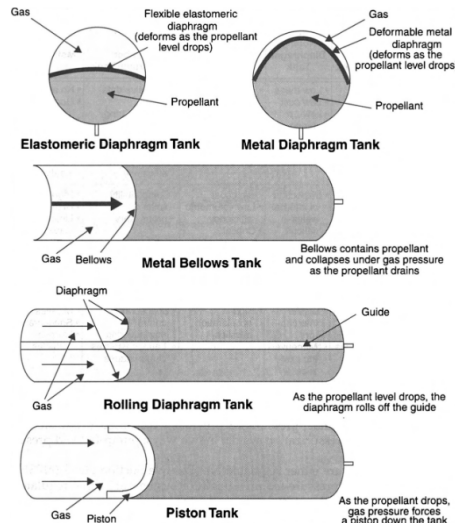


Figure 2: Positive expulsion Devices to Manage Propellant [20]

In this type of architecture there is no separated high-pressure gas tank and no pressure regulator. The expansion of the gas, already in the tanks, provides the expulsion of the propellants. Blowdown systems can be lighter than a regulated pressure system but gas temperatures, pressures and the resulting thrust all steadily decrease as propellants are consumed [41].

Different propellant-expulsion devices exist, positive or passive. Positive expulsion devices use physical barriers between propellant and pressurant gas, such as bladders, pistons, diaphragms and bellows [20]. Examples of positive expulsion devices are shown in Figure 2.

Regarding pressurizing gasses, two choices exist: helium (He) and nitrogen (N_2). Helium is much more expensive compared to nitrogen, despite offering better performances. In fact, helium is about seven times lighter than nitrogen and thus it is more advantageous for space applications in which lower masses are required, having as a drawback higher volumes. On the other hand, nitrogen is also prone to condensation under strong adiabatic expansions, whereas helium is not [41].

The valves and other components of the architecture are listed and further explained in Section 3.2.5.

2.3 Propellant overview

As stated by the **REQ-01**, the required propellant is the combination of liquid oxygen (*LOX*) and kerosene (*RP-1*). This formulation is a candidate propellant combination for launch vehicle booster rocket engines, such

as in the first stages of the Atlas, Delta, Titan 1 and Saturn launch vehicles.

The thrust values associated with this propellant combination are presented in Table 2.

Rocket	Atlas V	Delta II	Titan I	Saturn V
Thrust [kN]	3827	4822	1900	34020

Table 2: Examples of *LOX/RP-1* thrust values

It is worth noting that in the common application of this non hypergolic propellant-oxidizer pair, the thrust exceeds the levels stipulated by **REQ-02**, making the desired architecture unconventional. In scenarios where the required thrust is of a similar magnitude, for example in upper-stage applications, alternative propellant combinations such as liquid hydrogen and liquid oxygen (*LOX/LH₂*), or monomethylhydrazine and nitrogen tetroxide (*MMH/NTO*) are typically favoured [7]. This inclination towards them is due to their higher specific impulse, an indicator of the effectiveness of fuel consumption, and their ability to fulfil certain criteria like the capacity to restart the engine. Their compactness and volume efficiency make them suitable for smaller upper-stage propellant tanks.

The fuel in use is RP-1, a rocket-grade kerosene, characterized by its high energy density, superior compatibility with various materials, and the added advantage of a well-documented research history and extensive usage record. Despite RP-1 has lower specific impulse compared to other propellants like liquid hydrogen (*H₂*), it boasts several benefits including cost-effectiveness, stability at room temperature, and a reduced risk of explosion. As for the oxidizer, liquid oxygen (LOX) is employed. This is widely used in rocket propulsion systems due to its high oxygen content, which allows for combustion even in the absence of atmospheric oxygen - a critical requirement for space missions. LOX is stored and managed at ultra-low temperatures, typically around -183°C (90 K), where it remains in a liquid state, thus enabling efficient storage within rocket tanks and maximizing the quantity of oxidizer that can be carried onboard.

The properties of the propellant are shown in Table 3 [41] [12]:

	Density [kg/m ³]	Freezing point [K]	Boiling [K]	Specific heat [J/kgK]
LOX	1141	54.4	90.4	1673.6
RP-1	807	225	460-540	1882

Table 3: Properties of propellant

2.4 Material overview

A short overview on the materials used in the system is shown below.

2.4.1 Engine Material

In order to fulfil the **REQ-06**, the materials used to build the injector plate and the combustion chamber shall be fabricated using additive manufacturing (AM) processes . This requirement, together with the necessity of resisting the high temperature of the chamber, leads to the final choice of *Inconel 718*. This alloy is widely used in aerospace applications, plus it can be laser melted additively manufactured [22] [45] [24]. This material combines erosion resistance and high strength with outstanding weldability including resistance to postweld cracking: the tensile strength at high temperature ranges from 1200 MPa to 1400 MPa (this value can be influenced by factors such as manufacturing processes, heat treatments and microstructure) [8].

2.4.2 Thermal Barrier Coating

In order to withstand the high temperature inside the combustion chamber a thermal barrier coating (TBC) can be used (the cooling will be analysed in details in Section 3.4). TBCs consist of a layer of low-conductivity and high-temperature-resistant material deposited as a thermal protection on the inner side of the corrosion resistance barriers. The selection of TBC materials depends on several factors and on the requirements that must be satisfied [6]:

- **operating temperature range** ;
- **thermal conductivity**: low conductivity materials shall be used to provide effective insulation;
- **no phase transformation** between room temperature and operative temperature;
- **chemical inertness**: the material should resist oxidation, corrosion and chemical reactions;
- **adhesion to substrate**: the TBC must adhere well to the substrate material to prevent delamination. Various bond coat materials like *MCrAlY* (where M is usually nickel or cobalt) are used to improve adhesion;
- **low sintering rate** of the porous microstructure.

The most common used material is the ceramic Yttria-Stabilized Zirconia (YSZ). This material has already proved adequate adhesion with *Inconel 718* [10] and so it will be the one chosen and used in Section 3.4.

The 7–8 YSZ (7–8 mol % Y_2O_3 doping of ZrO_2) is the most popular investigated compositional range of YSZ used for numerous applications; it provides the best performance in high-temperature applications. The conductivity of the YSZ depends both from its microstructures and from its manufacturing process (APS, Atmospheric Plasma Spray, technique allows to achieve the lowest conductivity value with respect to the other technique) [42]. Although, a major disadvantage of YSZ is the limited operation temperature (<1473 K) for long-term application, due to phase transformation. In order to increase the range of operating time, the usage of hollow powders not only allows having a more efficient melting of zirconia ceramics, but also produces lower conductivity and more compliant coatings [11].

2.4.3 Tank Material

Concerning the material used for the tanks, although titanium is widely used in space applications, it must be avoided for storing liquid oxygen due to its sensitivity to corrosion [32]. The choice of material typically lies between iron and aluminum alloys. The latters are attractive candidates for pressure vessels because of their high strength-to-weight ratios, however, the majority of aluminum alloys used in the aerospace industry are not weldable. On the other hand, iron alloys are extensively used to build cryogenic tanks. Despite having higher density compared to aluminum alloys, steel offers a significant advantage in weldability for tank design.

The material chosen for the tank design is the *304 stainless steel* and the sizing is performed in Section 3.2.7.

2.5 Metallic additive manufacturing uncertainty

Additive manufacturing (AM) techniques have many advantages compared to standard manufacturing techniques, such as the ability to fabricate complex shapes impossible to fabricate with other methods. Various additive manufacturing techniques exists in the industry, each with their own advantages and disadvantages. For example, the NASA Marshall Space Flight Center (MSFC) has been employing powder-bed fusion or selective laser melting to build combustion chambers for motors in the range of 100 *lbf* to 35000 *lbf* (0.4 *kN* to 155 *kN*). Other techniques including laser Directed Energy Deposition (DED), arc-based deposition, and laser-wire cladding techniques have also been used to develop several components. [15]

The most common AM process is Powder-Bed Fusion (PBF), also known as Selective Laser Melting (SLM), which uses a layer-by-layer powder-bed approach in which the desired component features are sintered and subsequently solidified using a laser [15]. As shown in Figure 3, SLM techniques offers a high precision at the cost of a very low deposition rate.

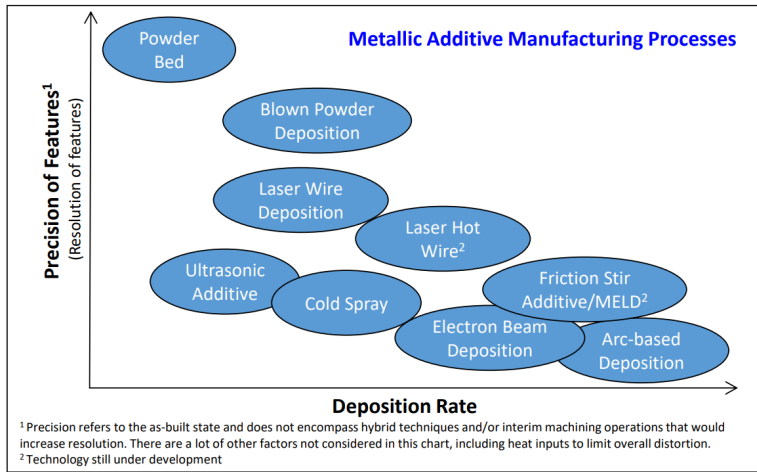


Figure 3: Comparison of Metallic Additive Manufacturing Processes [15]

One important disadvantage of SLM is its limited scale, as the majority of the SLM machines available for component fabrication are sized to accommodate 250 mm x 250 mm x 300 mm, but new machines are becoming available with up to 600 mm x 400 mm x 500 mm.

Regarding injector fabrication, the minimum hole size achievable using powder-bed fusion techniques is 200 μm [28]. Moreover, some of the specific disadvantages of using AM techniques to make these type of components are uncertainties in the resolution and excessive surface roughness. Another current disadvantage for the powder bed process in injector manufacture is the necessity to remove residual powder from internal passages where the part may have limited access. [15]

For the current analysis, resolution uncertainties influence the diameter of the injectors while an increased surface roughness influences the discharge coefficient C_D . In particular, C_D will decrease as the roughness increases [26]. In general, high accuracy and resolution can be obtained with AM [39] while surface roughness obtained is generally quite poor [13] with values ranging from 100 – 300 μm [29]. Typical values of uncertainties of AM techniques found in literature are reported in Table 4.

Parameter	Average value	Best case	Worst case
Accuracy	60 μm [28]	20 – 50 μm [28]	200 μm [9, table 2]
Variation of C_D due to roughness	7 – 8% [29]	4% [39]	14% [13]

Table 4: Additive manufacturing uncertainties in best, worst and average case scenario

Despite this, it is possible to notice from the formula used to calculate the mass flow rate \dot{m} through a circular injector 1, that the dependence on the C_D is linear while dependence on d_{inj} is quadratic.

$$\dot{m} = C_D \left(\frac{\pi d_{inj}^2}{4} \right) \sqrt{2\rho \Delta P} \quad (1)$$

This means that it is possible that the uncertainties of accuracy might have a higher impact compared to the variation of the C_D . Variations of propulsion parameters due to those uncertainties are further analyzed in Section 3.5.

3 Modelling approach

In this section, the modeling process adopted for the analysis is explored, offering a comprehensive overview of the methodologies, techniques, and theoretical foundations that support the followed approach.

3.1 Combustion and CEAM

The combustion process has been simulated using the NASA CEAM [14] (Chemical Equilibrium with Applications for MATLAB). The inputs are the following:

- P_c : combustion is defined by entering the pressure in the combustion chamber, retrieved from Subsection 3.3.
- O/F : required as the reactant amount defined in the *reactant dataset* is not in moles.
- ε_c : to define the combustion with finite chamber, to take into account the performance losses due to chamber velocity.
- ε : coupled with the keyword "sup", to compute the supersonic solution.
- *frozen*: no reactions happen in the nozzle, underestimating the real performances due to the absence of recombination processes in the nozzle.
- *transport*: to determine the transport phenomena of energy, momentum and mass when subjected to a temperature, pressure or concentration gradient. The retrieved thermodynamical properties are necessary to study the cooling analysed in Subsection 3.4.

To obtain the correct γ the Mayer relation should be used, starting from the knowledge of c_p and M_m . In addition, CEAM provides static thermodynamic quantities.

3.2 Sizing

3.2.1 Performance

The sizing starts from requirements listed in Table 1.1, therefore considering the nominal conditions as the initial ones.

In particular, a consideration on the initial thrust is made. Supposing that the required initial thrust of 1 kN (**REQ-02**) already needs to consider 2D losses, it is necessary to compute the ideal 1D thrust, needed to realize the sizing. To do that, an iterative process has been employed, starting with an assumption on the correction factor, granting the nozzle design which provides the real λ . The cycle was interrupted reaching a factor of 0.9872 and a 1D thrust of 1.0128 kN.

The expansion ratio ε is chosen considering the fact that the engine is used for an upper stage. These types of engines have a high area ratio, usually between 100 – 400. Since external pressure is zero, as the engine is operating in vacuum, choosing higher values of ε would achieve better performances, but, at the same time, a high area ratio increases mass, since the divergent is getting larger, and 2D losses are reducing progressively the benefit of the growth. As such, an intermediate ε of 200 was chosen.

Another input needed for sizing is the O/F ratio. This parameter has a direct impact on the specific impulse I_{sp} . It is possible to notice that the maximum vacuum I_{sp} is reached in the O/F range of 2.2 – 2.4. To determine exactly the optimal O/F ratio given the motor geometry, the I_{sp} is plotted as function of O/F as shown in Appendix B Figure 25 and the optimal O/F ratio of 2.2816 is chosen.

From CEAM simulation, as inputs specified in Subsection 3.1, thermodynamic quantities are retrieved, in particular in the combustion chamber, in the throat and at the nozzle exit. Attention is posed on the values referred to the combustion chamber, as only in this case total quantities are equal to static ones.

The pressure P_e at the nozzle exit is computed using the relation linking ε , P_c , γ to P_e , assuming an isoentropic ideal nozzle. The equation, however, has no closed-form solution, therefore it is solved numerically, using as initial guess the CEAM exit pressure.

It can be noticed that the pressure found (974.78 Pa) suggests that the ε chosen allows to largely expand the exhaust gases, ensuring a thrust close to the ideal maximum, achievable only with an optimal nozzle ($\varepsilon \rightarrow \infty$). The velocity u_e at the nozzle exit is computed through a relation linking combustion quantities and P_e . The high value found coupled with P_e , confirms that most of the thrust contribution comes from the dynamic part, rather than the static one.

The throat area A_t , the exit area A_e and the propellant mass flow rate \dot{m}_p can be computed by solving a system of three equations in 3 unknowns shown in Appendix A in 25. In particular, the three equations considered are the thrust equation, the definition of ε and the characteristic velocity c^* definition.

An important consideration must be done on the latter equation. c^* is a function of the propellant characteristics and combustion chamber design and it can be computed through two different formulas. The first version allows the determination of c^* from sensors data. The second version gives the ideal value of c^* as a function of

working gas properties, namely γ , T_f and M_m . It is possible to define the term c^* -efficiency in order to express the degree of completion of chemical energy releases in the generation of high-temperature, high-pressure gases in combustion chambers, which causes the two formulas to provide different values. This efficiency is computed as the ratio of the actual value of c^* , as determined from measurements, to the theoretical value. Although usually true, this difference is actually not being considered since the preliminary sizing is done with ideal conditions and the discrepancy emerges only on the experimental context.

At this point, the specific impulse I_{sp} is found equal to 353.86 s, a typical value for the mixture RP1-LOX[41]. Moreover, the thrust coefficient c_T is computed as well, equal to 1.9693, corresponding to the coefficient of merit of the divergent.

3.2.2 Nozzle

From the system of equations mentioned in Section 3.2.1, it is possible to compute the values of A_t and A_e . At this point, the lengths of the convergent and divergent parts for the nozzle are obtained starting from the semi aperture angles α and β , taken respectively as 15° and 45° . The first value is related to a reference conical nozzle which will be the starting point for the development of the Rao nozzle, as mentioned in Section 2.1.2, while the latter is a typical semi aperture angle of the convergent part.

It is now possible to size different versions of this type of nozzle by fixing the length of the divergent part as 100%, 80% and 60% of the reference conical model. The two parabola angles θ_i and θ_e for each possible nozzle are taken from graph 24 (since the chosen ε of 200 is not present in the graph, approximated values are taken). The choice of initial and final parabola angles for Rao nozzle, are shown in Appendix B, 24.

Finally, the correction factors of these three different versions and of the reference conical model are computed and compared, leading to the selection of the one whose length is 80% of the reference conical nozzle shown in Figure 4, as it represents the best trade off between performances and length, which is strictly related to the overall weight.

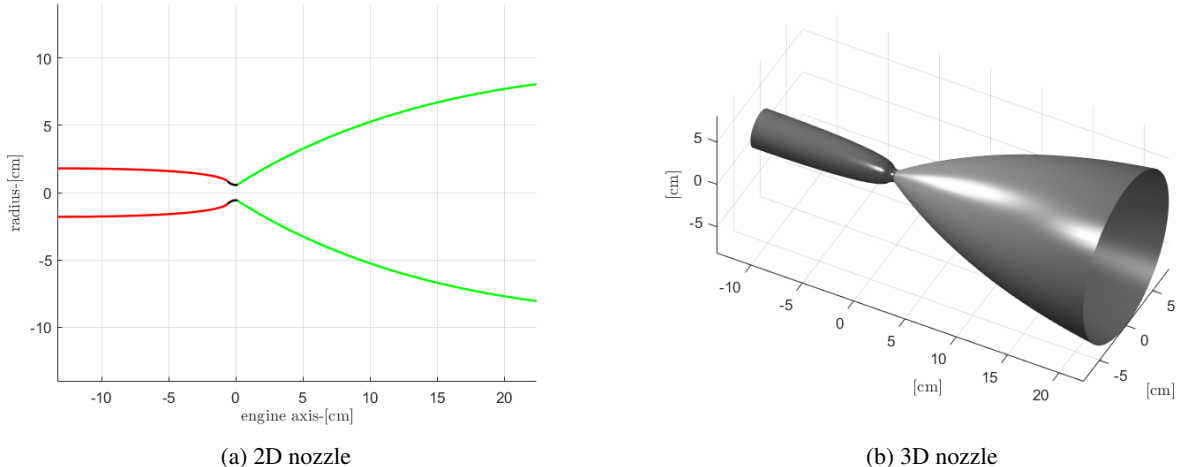


Figure 4: Rao nozzle with 80% length

2D losses of the conical and Rao nozzle are computed using the following equations:

$$\lambda_{conical} = \frac{1}{2} \left(1 + \cos \left(\frac{\alpha}{2} \right) \right) \quad \lambda_{Rao} = \frac{1}{2} \left(1 + \cos \left(\frac{\alpha + \theta_e}{2} \right) \right) \quad (2)$$

The parameters of the conical, 80%, and 100% length Rao nozzle are illustrated in Table 5, it is important to note that the length of the convergent is common to both nozzles and is 1.23 cm.

Nozzle type	Divergent length [cm]	2D losses coefficient [-]
Conical	28	0.983
80% Rao	22.4	0.9872
100% Rao	28	0.9925

Table 5: Length and 2D losses coefficient for 15° conical nozzle and both 80% and 100% length Rao nozzle

It is possible to notice that the 80% length Rao nozzle has an intermediate value of λ but has the advantage of having shorter divergent length, hence lower mass and reduced occupied volume.

3.2.3 Combustion Chamber

Apart from the hypotheses already mentioned in Section 3.1, the main constraint imposed to size the combustion chamber is to assure Mach M_c below 0.3, to avoid compressibility and combustion issues.

The sizing of the combustion chamber, which is assumed to be simply cylindrical, starts from contraction ratio ε_c and characteristic length L^* . Typical values of ε_c range between 5 – 15 while for L^* the LOX/RP-1 is in the range 1.02 – 1.27 m [20], as it depends on the specific couple of fuel and oxidizer. Knowing this, the value of ε_c is chosen as 10, since a low value of the contraction ratio results in a long and narrow combustion chamber. For L^* , on the other hand, the worst-case scenario of 1.27 m is considered. This choice is made since L^* is linearly dependent on the residence time, as such, a higher value of L^* ensures a sufficient residence time for the reaction to occur. Afterwards, the M_c is computed in order to verify that it is in the typical range of 0.1 – 0.3.

Another approach is attempted, starting from the M_c ; this method, however, is discarded since it produces unrealistic results, creating an unreasonably long and narrow combustion chamber, as shown in Figure 22, linked to an $\varepsilon_c = 3$.

3.2.4 Injector design

Before beginning the design of the injector plate, the first thing to notice is that the propellant pair does not ignite spontaneously. As such, it needs to absorb energy before the ignition occurs. This necessary energy is provided by the igniter, which is situated close to the injectors. In this design process, the initial transient phase is overlooked, and it is assumed that the initial ignition has already taken place.

The injection plate design starts from the values of \dot{m} and P_c : in order to achieve a reasonable number of holes, with such values, the short tube with the conical entrance is chosen as the orifice type 26, since it provides a wider range of options for the diameter. The design starts by deciding the diameter for the fuel orifices as well as their respective discharge coefficient. To adjust the number of orifices to be an integer, the O/F is changed to 2.352 by an iterative process. A triplet configuration is selected to better provide this ratio without changing the diameter of the orifices for the oxidizer, which results in being the same as the one for the fuel. Another advantage of this layout resides in the fact that, due to the symmetry, the conservation of momentum is always satisfied and the angle of the propellant will always be 0° , providing an axial flux. The configuration is a like impinging one and the pressure drop is hypothesized to be 25% of P_c .

Parameter	Symbol	Value for LOX	Value for RP-1	Unit
Number of orifices	N	28	14	–
Diameter of orifices	d	0.5	0.5	mm
Discharge coefficient	C_d	0.69	0.7	–
Injection angle	δ	45	0	°

Table 6: Values for the injection plate

As it can be observed from Table 6 the diameter of the orifices respects the constraints on the minimum accuracy due to the AM technique, satisfying the **REQ-06**, which is of primary concern for the design. The injection angle for the oxidizer is also chosen to satisfy the minimum building angle, common to metal AM machines [4].

After the initial sizing it is also verified that the total area of the fuel and oxidizer orifices is less than the one of the combustion chamber and, on top of this, the impingement point is also calculated to be 3 mm. The atomization happens right after the injection and its performance is influenced by the size of the droplets produced from the injector. For this end, Sauter Mean Diameter (SMD) is used as an estimator which generally depends on Reynold's and Weber's numbers [1]. For both fuel and oxidizer:

$$\begin{cases} Re & = \frac{\rho u D_{\text{orifice}}}{\mu} \\ We & = \frac{\rho u^2 D_{\text{orifice}}}{\sigma_{\text{st}}} \\ SMD & = D_{\text{orifice}} \cdot 82.23 \cdot C_d^{0.64} \cdot We^{-0.07} \cdot Re^{-0.5} \end{cases} \quad (3)$$

where the surface tension σ_{st} [5] and the molar volume V_{mol} are computed as follows:

$$\begin{cases} \sigma_{\text{st}} & = \frac{k_{Eot}(T_{RP1_{\text{critic}}}-T_{\text{stored}})}{V_{\text{mol}}^{2/3}} \\ V_{\text{mol}} & = \frac{MM}{\rho} \end{cases} \quad (4)$$

As expected from the reduced size of the engine, the SMD is very small due to the high value of We and Re for both LOX and RP-1. As a matter of fact, the breakage of particles is initiated by inertial and drag forces countered by surface tension and viscosity. In addition, it can be noticed that RP-1 is characterized by an SMD one order lower than that of LOX as its viscosity is much higher.

Input			
RP-1 storage temperature	$T_{RP1_{\text{stored}}}$	300	K
LOX storage temperature	$T_{LOX_{\text{stored}}}$	90	K
RP-1 critical temperature	$T_{RP1_{\text{critic}}}$	425	K
LOX critical temperature	$T_{LOX_{\text{critic}}}$	154.58	K
RP-1 molar mass ¹	MM_{RP1}	0.175	kg/mol
LOX molar mass	MM_{LOX}	0.0320	kg/mol
RP-1 liquid density	ρ_{RP1}	810	kg/m ³
LOX density	ρ_{LOX}	1140	kg/m ³
Eotvos coefficient	k_{Eot}	$2.1 \cdot 10^{-7}$	J/(K * mol ^{2/3})
RP-1 injection velocity	u_{RP1}	27.5	m/s
LOX injection velocity	u_{LOX}	23	m/s
RP-1 dynamic viscosity @ $T_{RP1_{\text{stored}}}, P_{RP1_{\text{stored}}}$	μ_{RP1}	$1.4 \cdot 10^{-3}$ [33]	Pa·s
LOX dynamic viscosity @ $T_{LOX_{\text{stored}}}, P_{LOX_{\text{stored}}}$	μ_{LOX}	$6.79 \cdot 10^{-6}$ [18]	Pa·s

Table 7: Atomization input data

Output			
RP-1 superficial tension	$\sigma_{st_{RP1}}$	0.0073	N/m
LOX superficial tension	$\sigma_{st_{LOX}}$	0.0147	N/m
RP-1 Weber	We_{RP1}	$42.011 \cdot 10^3$	-
LOX Weber	We_{LOX}	$20.54 \cdot 10^3$	-
RP-1 Reynolds	Re_{RP1}	$7.697 \cdot 10^3$	-
LOX Reynolds	Re_{LOX}	$1.9308 \cdot 10^6$	-
RP-1 Sauter Mean Diameter	SMD_{RP1}	$1.7704 \cdot 10^{-4}$	m
LOX Sauter Mean Diameter	SMD_{LOX}	$1.1645 \cdot 10^{-5}$	m

Table 8: Atomization output data

¹Kerosene C_4H_{10} is used for molar mass and critical temperature values [31] in a first approximation.

3.2.5 Feeding Architecture and Pressure Drop

The feeding line design is necessary to compute the initial pressure in the oxidizer and fuel tank, to then estimate the volume and mass amounts. The first assumption made regards the pipes diameter choice, using the continuity equation and supposing the pipes velocity $u_p = 15\text{ m/s}$. This design choice is based on the necessity to guarantee a proper velocity in the pipes at the end of burning time, assuring always a correct supply. Furthermore, the choice of a greater value of u_p is necessary to respect the quick flow constrain to ensure the assumption of adiabatic expansion of the pressurizing gas in the nozzle. To work properly, the feeding line requires for each branch:

- **fill and drain valve**: necessary to maintain low leak rates and grant propellant loading and venting;
- **latch valve**: solenoid valves that offer bi-stable valve operation by utilizing a permanent magnet to maintain the valve in both the open and closed position while under pressure. This removes the need for electrical power to hold the valve open or closed [25];
- **check valve**: to prevent backflow;
- **filter**: to prevent impurities to enter the pipe line and is designed to avoid to blocking itself.
- **pressure and temperature transducer**: to avoid dangerous non-nominal condition in the feeding line.

A general architecture of the feeding lines is illustrated in Figure 5.

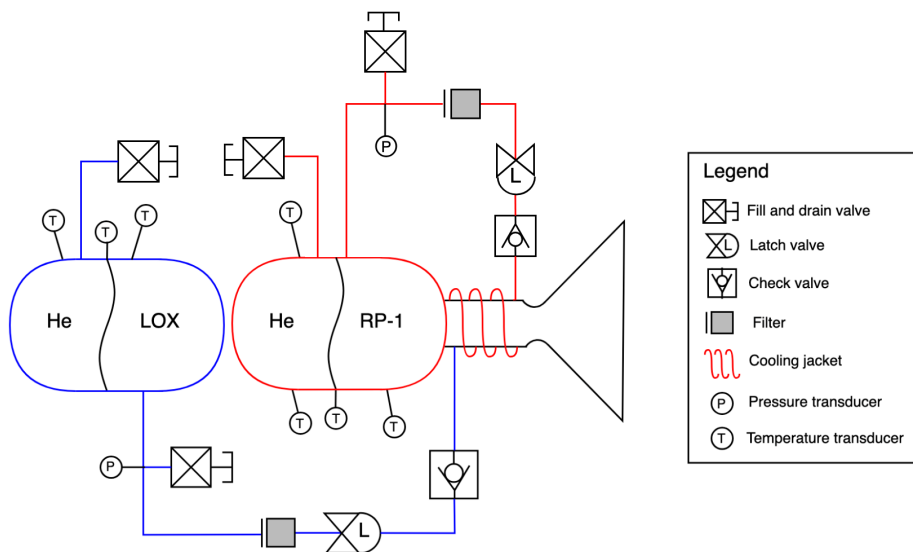


Figure 5: Qualitative representation of the feeding line architecture.

To compute the pressure in the tanks, with the hypothesis made in Section 3.3, it is necessary to evaluate the pressure drop from the tanks to the combustion chamber, with the assumption made in Section 3.3. The real pressure cascade is computed as:

$$P_t - P_c = \Delta P_{dyn,t} + \Delta P_{dis} + \Delta P_{conc} + \Delta P_{inj} \quad (5)$$

The qualitative pressure losses as function of the length of the feeding lines is illustrated in Figure 6.

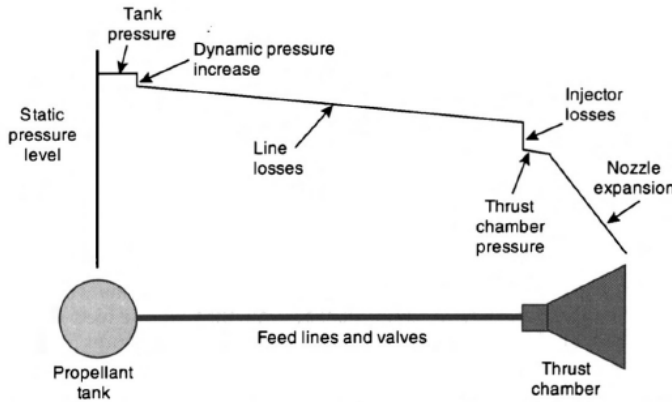


Figure 6: Qualitative pressure cascade [20]

Since in this report only a preliminary sizing is performed, the exact length and properties of both feeding lines and valves are not known at this stage, as such, it is not possible to quantify the exact value of distributed and concentrated losses. Consequently, a worst case scenario is considered, where the concentrated pressure drops are assumed to be 50 kPa.

$$P_t - P_c = \Delta P_{dyn} + \Delta P_{feed} + \Delta P_{inj} \quad (6)$$

It's interesting to highlight that the initial tank pressure is different for LOX and RP1 due to their different density and mass flow rate in the pipes. Moreover, the initial pressure in the tanks depends only on the initial conditions and performances and not on the burning time nor on stored LOX and RP1 masses. Concerning the pressure drops due to cooling, they are not considered as the feasibility of regenerative cooling is not yet known at this stage. A more in-depth analysis of the cooling system is performed in Section 3.4.2.

3.2.6 Blowdown ratio and Propellant quantity estimation

- **Pressurizing gas choice:**

As stated in Section 2.2, helium is much more desirable compared to nitrogen, being much lighter. As such, helium is chosen as pressurizing gas.

It is assumed that the helium is loaded in the tanks at an initial temperature of 273.15 K, an usual temperature for space applications as reported in [44]; the second assumption is that helium is treated as a perfect gas so it is straightforward to notice that the initial temperature impacts only the helium mass required and the temperature profile along the mission.

Despite this, it is important to take into account the fact that LOX is cryogenic: having helium at relatively high temperature in close proximity with cryogenic LOX could bring issues related to excessive boil-off of the cryogenic propellant. Therefore, helium at a pressure of 90 K is also considered. A comparison between the two choices is made in Section 3.2.7.

- **Blowdown Ratio choice:**

The first and fundamental design parameter of the analyzed system is the blowdown ratio B , which is the pressure ratio between the P_{He} in the tank at the beginning of the transformation and at the end. Furthermore, under the hypothesis of adiabatic expansion of the helium, the B can be expressed as the final helium volume over the initial one, all raised to γ .

The adiabatic expansion assumption holds in case of quick transformation, not allowing the gas to reach the thermal equilibrium. In order to avoid a major decrement of pressure in tanks and so in the combustion chamber, to avoid an important drop of performances in time, the blowdown ratio cannot be too high. To determine a qualitative interval of B , it is performed a rough estimation starting from the initial and minimum pressure in the combustion chamber, as P_c is an indication of the pressure in the tanks P_t ; another qualitative lower bound is found by computing backwards the pressure cascade from the combustion chamber, with the minimum allowed pressure $P_c = 20 \text{ bar}$, finding an initial guess of the final pressure in the tanks and, thanks to the fact that the initial pressure in the tanks is constrained by

the performances and sized architecture. As previously stated, being B a design parameter, all the system adapts to it, to match the condition imposed, as further said in Subsection 3.3. For simplicity, B is chosen equal for both the oxidizer and fuel tank.

- **Tanks Volume Ratio choice:**

The second constraint on the design is dictated by the necessity of fixing a parameter from which it is then possible to compute the remaining unknown extensive quantities: this value is the O/F ratio. To achieve this, it is necessary to employ an iterative process that solves several equations, as demonstrated in Appendix 5. The system involves adiabatic equations for both the propellant and two volume equations in order to satisfy the constraint on the engine dimensions. The main goal of this process is to ensure that there is no residual propellant after combustion to avoid wastage. To achieve this, the available volume for the propellant tanks is calculated as $V_{\text{tank}} = 0.8V_{\text{available}} - V_{\text{cc}}$, where the dimensions of the entire engine $V_{\text{available}}$ must satisfy **REQ-04**. The step of each iteration is defined within a range of values for $\frac{V_{\text{ox}}}{V_{\text{fuel}}}$. By solving the system, the initial and final volumes of helium for both the oxidizer and fuel tanks, along with the final temperature of the pressurizing gas, can be determined. Additionally, at each step, the value of O/F can be obtained using the quantities listed above; specifically, the volume allows for the calculation of the mass of oxidizer and fuel.

Given that the mass flow rate of the two propellants cannot have a linear relation over time (due to $\dot{m} \propto \sqrt{\Delta p}$, where the pressure losses change with time), in a first evaluation, O/F can be estimated as the ratio of the masses of oxidizer and fuel. The value determined at each iteration is considered as mean value of the actual ratio, but it holds fundamental significance in the preliminary design phase.

Both the last two points are based on a *trial and error* mechanism in which the independent parameters are changed and chosen to satisfy the imposed constraints, shown in the Appendix A 5: regarding the blowdown ratio, the value that allows for respecting performance parameter trends shown in literature, while depleting the propellants, is $B = 2.1$.

For the O/F ratio, since the mass flow rate does not follow a linear trend as previously mentioned, the mean O/F obtained appears to be lower than the arithmetic mean value. Because of this, the selected value for proceeding with the design is slightly lower than the arithmetic mean value, $O/F = 2.3167$.

3.2.7 Tank Sizing

To size the tanks, the following assumptions are made:

- liquid propellants are considered incompressible;
- tanks are assumed to be cylindrical, without considering eventual hemispherical domes;
- the two tanks are considered to be in tandem, with their diameter equal to the diameter of the total available space (1 m);
- diaphragm volume is supposed to be negligible;
- the pressurizing gas is supposed to follow an adiabatic transformation and, consequently, both the tanks and diaphragms are considered well insulated and adiabatic;
- the liquid propellant and the pressurizing gas are supposed to be at the same pressure;
- diaphragms behaviour is considered ideal: it is assumed that at the end of the burn, the pressurizing gas will occupy the entire volume of the tank.

As mentioned in Section 2.4.3, the chosen material is stainless steel 304. Its properties are: ultimate tensile strength σ of 505 MPa and density ρ of 8000 kg/m³ [19].

To compute the wall thickness and mass of the tank, the equations in Appendix A 26. The main characteristics of the tanks are listed in Table 9:

Propellant	Initial pressure [bar]	Height [m]	Wall thickness [mm]	Tank mass [kg]
LOX	64.28	0.9983	6.3	160.71
RP-1	63.91	0.6015	6.4	96.26

Table 9: Parameters of the LOX and RP-1 tanks.

Concerning the pressurizing gas, for the LOX tank, a comparison is made in 10, for RP-1, instead, a mass of 3.41 kg is obtained, considering an initial temperature of 273.15 K.

Temperature [K]	Mass [kg]	Density [kg/m ³]
90	17.29	34.38
273.15	5.7	11.33

Table 10: Helium mass and density for 90 K and 273.15 K storage.

It is straightforward to notice that, if helium is loaded at a higher temperature, the required mass needed to pressurize the tank is significantly lower. On the other hand, as previously mentioned, having helium at cryogenic temperature is better to avoid boil-off of the LOX. One disadvantage of the latter, however, is that, while helium is definitely in the gaseous phase at 90 K and 64.28 bar [16, p. 90], some problems may arise towards the end of the burn when the gas has expanded if a real and non-adiabatic transformation is considered instead. As such, while a lower temperature for helium could be advantageous for the presented system, further analyses need to be performed using more accurate models and empirical data.

3.2.8 Sizing results

The analysis leads to the results shown in Tables 11 and 12:

	M [kg]	V [L]	T [K]	P [bar]
LOX	320.66	281.2	90	64.28
RP1	137.25	169.5	300	63.91
He for LOX	5.69	502.9	273.15	64.28
He for RP1	3.41	169.5	273.15	63.91

Table 11: Initial mass, volume, temperature and pressure of LOX, RP1, and He of both tanks.

The masses of oxidizer and fuel found are only constrained by the choice of B and $K = \frac{V_{tank,Ox}}{V_{tank,fu}}$, whereas the helium mass, which remains constant during the mission for principle of conservation of mass, depends only on the initial temperature.

	Diameter [cm]	Length [cm]
Combustion chamber	3.6	12.7
Nozzle's Convergent	1.14	1.23
Nozzle's Divergent	16.14	22.39
Oxygen tank	100	99.83
Fuel tank	100	60.15

Table 12: Dimensions of the whole system.

From Table 12, it is possible to see that the overall length of the combustion chamber, convergent and both tank is 1.73 m meaning that the complete system fits inside the allocated maximum length of 2 m, respecting **REQ-04**, allowing to take into account the footprint of the tanks domes and feeding lines.

The engine and the tanks are qualitatively represented in Figure 7.

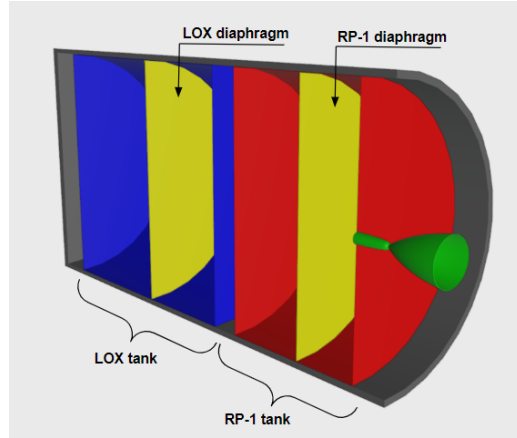


Figure 7: Qualitative 3D render of the complete system.

By looking at the proportions of tanks and the engine, the system is expected to have a low thrust engine with a relatively high burning time. This consideration is later analysed in Subsection 4.1.

3.3 Blowdown cycle

The blowdown computational cycle *rationale* lies in the time and space separation, that occurs between the tanks and the combustion chamber. Physically, the discharged mass from the tanks at a determined instant influences the combustion chamber at the following moment in time, since fuel and oxidizer masses require time to cover the spacial distance. Starting from this consideration and discretizing the phenomenon for the i -th time step dt , the mass flow rate that influences the performances in the combustion chamber at a time step i is ejected from the tanks at the previous time step $i - 1$. The following Figure 8 clarifies what has been explained:

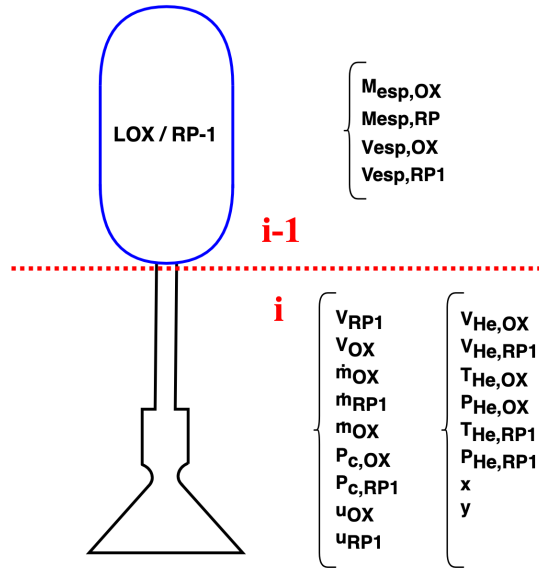


Figure 8: Visual representation of time and space computational separation

Therefore, the expelled oxidizer and fuel masses and volumes can be computed as:

$$M_{esp,OX}(i-1) = \dot{m}_{OX}(i)dt \quad M_{esp,F}(i-1) = \dot{m}_F(i)dt \quad (7)$$

$$V_{esp,OX}(i-1) = \frac{M_{esp,OX}(i-1)}{\rho_{OX}} \quad V_{esp,F}(i-1) = \frac{M_{esp,F}(i-1)}{\rho_F} \quad (8)$$

Where $\dot{m}_{OX}(i)$ and $\dot{m}_F(i)$ are the mass flow rates of fuel and oxidizer, respectively. They are considered at

the time instant i , since those are the mass flow rates that influence the combustion chamber performances. Moreover, ρ_{OX} and ρ_F are the densities of the oxidizer and fuel, which are assumed constant for the mission considered. This is a consequence of the hypothesis of neglecting the compressibility effects, reasonable in this case since the Mach number is under the value of 0.3 [34] in the feeding line and tanks. The volumes of pressurizing gas in oxidizer and fuel tanks and oxidizer and fuel themselves can be computed as:

$$V_{He,OX}(i) = V_{He,OX}(i-1) + V_{esp,OX}(i-1) \quad V_{He,F}(i) = V_{He,F}(i-1) + V_{esp,F}(i-1) \quad (9)$$

$$V_{OX}(i) = V_{OX}(i-1) - V_{esp,OX}(i-1) \quad V_F(i) = V_F(i-1) - V_{esp,F}(i-1) \quad (10)$$

All the introduced quantities are referred to the i -th time instant for the computational upgrade of the variables. Physically, they must be considered as the volumes that influence the combustion chamber performances, not properly the volumes in the tanks at the i -th instant.

The pressurizing gas in the tanks is hypothesised ideal and undergoes an adiabatic process [41]. Therefore, those additional equations can be used to model the blowdown of the tanks:

$$T_{He,OX}(i-1)V_{He,OX}(i-1)^{(\gamma_{He}-1)} = T_{He,OX}(i)V_{He,OX}(i)^{\gamma_{He}-1} \quad (11)$$

$$P_{He,OX}(i)V_{He,OX}(i) = M_{He,OX} \frac{R}{Mm_{He}} T_{He,OX}(i) \quad (12)$$

$$T_{He,F}(i-1)V_{He,F}(i-1)^{(\gamma_{He}-1)} = T_{He,F}(i)V_{He,F}(i)^{\gamma_{He}-1} \quad (13)$$

$$P_{He,F}(i)V_{He,F}(i) = M_{He,F} \frac{R}{Mm_{He}} T_{He,F}(i) \quad (14)$$

Where $T_{He,F}$ and $T_{He,OX}$ are the static temperatures of pressurizing gas in the fuel and oxidizer tanks, respectively. While, $P_{He,F}$ and $P_{He,OX}$ are the relative static pressures. $M_{He,OX}$ and $M_{He,F}$ are the masses of helium in oxidizer and fuel tanks, which are reasonably hypothesised constant all over the mission and equal to the design value (Section 3.2). This assumption is maintained also for the specific heat ratio of the gas γ_{He} , directly derived from the ideal gas hypothesis. R is the universal gas constant and Mm_{He} is the helium molar mass. It can be noticed that those equations are the links between the previous and current steps.

Considering the system isolated and fair-minded in the case analysed, the mass conservation law is valid, thus also the continuity equation can be applied for the pipes [35]:

$$u_{OX}(i) = \frac{\dot{m}_{OX}(i)}{\rho_{OX}A_{OX}^{pipe}} \quad u_F(i) = \frac{\dot{m}_F(i)}{\rho_F A_F^{pipe}} \quad (15)$$

u_{OX} and u_F are the velocities associated with oxidizer and fuel pipes, while A_{OX}^{pipe} and A_F^{pipe} are the area of the pipes, calculated at Section 3.2.

The pressure in the tanks P_t must be equal to the sum of the chamber pressure P_c and all the pressure drops through the feed system [20] both for oxidizer and fuel pipelines:

$$P_{tank}(i) = P_c(i) + \Delta P_{dynamic}(i) + \Delta P_{feed} + \Delta P_{cool} + \Delta P_{inj}(i)$$

Following the model developed, the quantities marked with index i are time-varying, while the others are assumed constant. Analyzing deeply the terms in the previous equation:

- $\Delta P_{dynamic}$: as the propellant exits the tank, its velocity transitions from zero to the required flow velocity. Initially, the total pressure remains approximately constant, especially over the initial short distance. Consequently, the static pressure decreases to accommodate the rise in dynamic pressure. In the case of incompressible flow, which adequately describes most liquids, the pressure reduction resulting from the increase in dynamic pressure is quantified by Bernoulli's equation. Computing them for fuel and oxidizer:

$$\Delta P_{dynamic,OX}(i) = \frac{1}{2}\rho_{OX}u_{OX}(i)^2 \quad \Delta P_{dynamic,F}(i) = \frac{1}{2}\rho_F u_F(i)^2$$

Where $u_{OX}(i)$ and $u_F(i)$ are the velocities in the pipelines of fuel and oxidizer at the instant i ;

- ΔP_{feed} : from literature [20] the pressure drops due to the feeding line are usually between 35,000 Pa and 50,000 Pa. To be conservative, the value $\Delta P_{feed} = 50,000$ Pa is used;

- ΔP_{cool} : the losses due to the cooling system are imposed null since it is not considered in the nominal design;
- ΔP_{inj} : those are the losses due to the injection, which are considered for both lines in the following way:

$$\Delta P_{inj,OX} = x(i)P_{c,OX}(i) \quad \Delta P_{inj,F} = y(i)P_{c,F}(i)$$

In the previous equations $\Delta P_{inj,OX}$, and $\Delta P_{inj,F}$ are the feeding losses for oxidizer and fuel pipes. $P_{c,OX}$ and $P_{c,F}$ are the combustion chamber pressure coming from the oxidizer and fuel lines. As will be explained, those pressures must be equal. $x(i)$ and $y(i)$ are the percentage of injection losses with respect to the combustion chamber pressure. Those are assumed time-varying (as the indices i mark), since at each iteration step the pressure in the injectors will be different to match time-varying the boundary conditions between before and after them. Initial values are set to $x(i) = 25\%$ and $y(i) = 25\%$, which follows the conservative philosophy chosen for this design [20].

Customising the equation previously written for oxidizer and fuel lines:

$$P_{He,OX}(i) = P_{c,OX}(i) + \frac{1}{2}\rho_{OX}u_{OX}(i)^2 + \Delta P_{feed} + x(i)P_{c,OX}(i) \quad (16)$$

$$P_{He,F}(i) = P_{c,F}(i) + \frac{1}{2}\rho_F u_F(i)^2 + \Delta P_{feed} + y(i)P_{c,F}(i) \quad (17)$$

Notice that the tanks pressures are considered equal to the pressure of the pressurizing gases, which are assumed in mechanical equilibrium with the pressure of the fluids. Moreover, $P_{c,OX}(i)$ and $P_{c,F}(i)$ are the instantaneous combustion chamber pressure merging from the oxidizer and fuel lines, thus those boundary conditions must be matched:

$$P_{c,OX}(i) = P_{c,F}(i) \quad (18)$$

Additional equations can be found from the pressure drop across the injectors. For the flow of an incompressible fluid through hydraulic orifices [41]:

$$\dot{m}_{OX}(i) = C_{D,OX}A_{OX}^{inj} \sqrt{2\rho_{OX}\Delta P_{inj,OX}} \quad \text{with } \Delta P_{inj,OX} = x(i)P_{c,OX}(i) \quad (19)$$

$$\dot{m}_F(i) = C_{D,F}A_F^{inj} \sqrt{2\rho_F\Delta P_{inj,F}} \quad \text{with } \Delta P_{inj,F} = y(i)P_{c,F}(i) \quad (20)$$

The A_{OX}^{inj} and A_F^{inj} are the total areas associated with the injectors of oxidizer and fuel determined in Section 3.2 and constant all over the cycle. Notice that the dimensionless discharge coefficients associated with oxygen $C_{D,OX}$ and fuel $C_{D,F}$ injectors are considered constant all over the mission time. From this consideration and analysing equations 19 and 20, it is evident that the time-varying matching between the pressures before and after the injectors is ensured by the varying $x(i)$ and $y(i)$.

The total mass flow rate of propellant is:

$$\dot{m}_p(i) = \dot{m}_{OX}(i) + \dot{m}_F(i) \quad (21)$$

To ensure the correct working of the nozzle, it is important to impose the sonic condition at the throat:

$$M_t(i) = \frac{u_t(i)}{a_t(i)} = 1$$

Where u_t is the velocity of the combustion gases in the throat and a_t is the sonic velocity at the throat. From the definition of the sonic velocity:

$$a_t = \sqrt{\gamma_{GC}(i-1) \frac{R}{Mm_{GC}(i-1)} T_{GC}(i-1)}$$

The $\gamma_{GC}(i-1)$, $Mm_{GC}(i-1)$ and $T_{GC}(i-1)$ are the specific heat ratio, the molar mass and the static temperature of the combustion gases, respectively. Those parameters are properly derived from CEAM run, but referred to the previous iteration. This enhances the computational efficiency of the code implemented and it is reasonable

since the time step chosen dt is small. The velocity of the combustion gases can be retrieved from the continuity equation in the throat:

$$\dot{m}_p(i) = \rho_{GC,t}(i-1)A_t u_t(i)$$

Where A_t is the throat area and $\rho_{GC,t}(i-1)$ is the density of combustion gases at the throat referred to the previous time step. It can be noticed that in the throat the flow conditions are so that the fluid cannot be considered incompressible, so a time-varying of the density must be taken into account.

Properly substituting the quantities in Mach definition at the throat, the following is obtained:

$$M_t(i) = \frac{\frac{\dot{m}_p(i)}{\rho_{GC,t}(i-1)A_t}}{\sqrt{\gamma_{GC}(i-1) \frac{R}{Mm_{GC}(i-1)} T_{GC}(i-1)}} = 1 \quad (22)$$

By solving the system of 21 equations in 21 unknowns (28) through MATLAB, it is possible to determine its quantities completely. The full system and the unknowns are highlighted in Appendix A 5.

After the system is solved, $O/F(i)$ is computed, so CEAM analysis is run with inputs $P_c(i)$ and $O/F(i)$. From CEAM outputs and in analogy to Section 3.2.1, the performances and exit conditions are calculated. Between those quantities, there is the Mach number at the throat. This is computed to verify the propagation error of the code, as it is useful to choose the correct time step dt . Quantities useful to restart the cycle are computed too.

The cycle is performed until at least one of the following conditions is verified:

$$M_{esp,tot,ox}(i) \geq M_{i,ox} \quad \vee \quad M_{esp,tot,f}(i) \geq M_{i,fu} \quad \vee \quad P_c(i) \leq P_{c,min} \quad \vee \quad M_{cc}(i) \geq M_{max} \quad (23)$$

The $M_{esp,tot,ox}(i)$ and $M_{esp,tot,f}(i)$ is the sum of the masses expelled from the initial instant from oxidizer and fuel tanks. While $M_{i,ox}$ and $M_{i,f}$ are the initial mass value of oxidizer and fuel. Physically, the first two conditions are equal to imposing that the total expelled masses do not exceed the available ones. The third condition corresponds to imposing that the pressure in the combustion chamber is always greater than the minimum value $P_{c,min} = 20$ bar that allows the combustion. The fourth condition is equal to fixing a maximum value to Mach number in combustion chamber of $M_{max} = 0.3$, which is set to avoid combustion problems, such as turbulence and compressibility effects.

As a concluding note, it is significant to emphasize that the iteration time step dt is lowered during the initial and final iterations to better simulate those moments. This approach is justified because: at the outset, the system needs to adjust to the initial conditions, necessitating precise monitoring of quantities variation; likewise, at the conclusion, it is crucial to precisely match the exit conditions to avoid exceeding physical limits and compromising the system delicate operation. The exit time from the cycle is evaluated to be the burning time t_b .

3.4 Engine cooling

The wall temperature of the combustion chamber and nozzle must be maintained at a safe level to avoid any structural failure. In the design phase, a simplified verification is made, considering the conservation of heat flux from the gas of the combustion chamber to the outside of its wall. Then, two cooling mechanisms are analyzed: radiation and regenerative cooling. The thermal analysis uses as input the properties of the gas from CEAM, *Inconel 718* and assumptions on the desired values.

Input			
Prandtl number in CC	Pr_g	0.6264	-
Thermal conductivity of gas	k_g	0.359	W/mK
Dynamic viscosity	μ	2.086	kg/ms
External temperature	T_{ext}	4	K
Wall thickness	t_{wall}	5	mm
Inconel 718 thermal conductivity	$k_{inc718-1000K}$	22	W/mK
Inconel 718 maximum temperature	$T_{inc718,max}$	973 [8]	K
Inconel 718 emissivity	ϵ_{In718}	0.25 [23]	-
RP-1 specific heat	$C_{P_{RP1}}$	1880	J/kgK
Isentropic expansion factor	γ_{cc}	1.22	-
Mach in combustion chamber	M_{cc}	0.0591	-
RP-1 boiling temperature	$T_{RP1,boil}$	460 – 540	K
RP-1 stored temperature	$T_{RP1,stored}$	300	K
YSZ thermal conductivity	$k_{YSZ-1000K}$	2.3 [47]	W/mK

Table 13: Cooling input

3.4.1 Radiative cooling

To develop the model, radiative cooling is assumed uniformly performed at the surface of the cylinder and the heat is exchanged with a surrounding environment at T_{ext} . Due to the low emissivity of *Inconel 718*, the temperature of the cold and hot sides of the wall is very high, reaching, respectively, 2888.8 K and 3113.2 K , which would be unsustainable for *Inconel 718*. These results are obtained with an initial guess of T_{wh} in the interactive process in which the equality of the two heat fluxes $q_1 = q_2 = q$ is verified.

$T_{wh} [K]$	$T_{wc} [K]$	$q [W/m^2]$
3113.2	2888.8	$9.8718 \cdot 10^5$

Table 14: Radiative cooling

3.4.2 Cooling Jacket with RP-1

Regarding the cooling jacket, the objective is to verify that there is enough propellant to remove heat, defined as the global problem. One limitation of utilizing kerosene and similar hydrocarbon fuels in regenerative cooling systems is that they can only effectively cool the engine until the fuel temperature surpasses its thermal decomposition, commonly referred to as the "coking" temperature [37]. At this point, deposits begin to form on the inner surfaces of the coolant walls. These deposits lead to a rise in thermal resistance, causing the coolant walls to experience increasingly higher temperatures, ultimately resulting in system failure.

Starting the design, considering a conservative approach the desired T_{wh} is assumed to be 1500 K and an adiabatic wall temperature of 3565.6 K , which is computed starting from the data obtained from the combustion chamber analysis.

The value of the final temperature that RP-1 should reach in order to guarantee the cooling is found to be 698.5 K , that is much higher than the boiling temperature of the fuel itself. Therefore, even if locally the situation is safe for the structure, which has a functional temperature that can go beyond 900 K , it is critical for the fuel point of view.

It has to be noted that the nozzle is not considered in this preliminary verification since the maximum heat flux happens slightly before the throat, so if the cooling mechanism is not able to cool down in the combustion chamber, it would not be able to do so in the nozzle.

3.4.3 Alternative solution

Since the result obtained in Subsection 3.4.2 suggests that the mass flow rate of the RP-1 is not capable of cooling the combustion chamber, a thermal coating is introduced in order to try to reduce the heat flux across the section of the engine. As a first approach to compute it, a thermal nodal model is chosen as shown in Figure 9

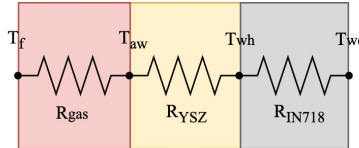


Figure 9: Equivalent electric circuit of the heat transfer model

The overall thermal resistance across the section is calculated considering in series the thermal resistance of the coating and the reciprocal of the convection heat transfer coefficient:

$$H_{\text{global}} = \frac{1}{\frac{1}{h_g} + \frac{t_{\text{YSZ}}}{k_{\text{YSZ}}} + \frac{t_{\text{wall}}}{k_{\text{inc718}}}} \quad (24)$$

As a small variation of the geometry of the propulsion system, e.g. changing the contraction ratio, would influence the whole design, a TBC is adopted selecting *Yttria-stabilized Zirconia* (YSZ), as seen in Subsection 2.4.2. An iterative process has been applied to plot the thickness of the coating in function of the maximum temperature ΔT_{\max} that can be subtracted by the coolant, obtained as the difference between the $T_{RP1_{boil}}$ and the $T_{RP1_{stored}}$. Consequently, the thickness of the coating is estimated to be $425 \mu\text{m}$ using a graphical approach in Figure 10, by considering a ΔT_{\max} of 210K , meaning that RP-1 reaches a temperature of 510K , that correctly falls below its boiling temperatures range, guaranteeing safeness. In general, the value of the TBC thickness must remain within the range of $100 - 500 \mu\text{m}$, as having a higher value would result in creating cracks between the TBC and the *Inconel 718* [43].

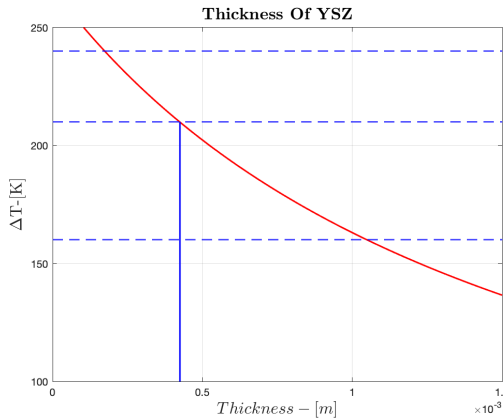


Figure 10: Dependency of the t_{YSZ} on the ΔT

3.5 Additive manufacturing variations

As stated in Section 2.5, AM techniques imply variations in performance due to differences in both roughness and accuracy of the diameter of the injector heads. To analyze which parameter influences the performance of the engine the most, an average case scenario is considered, using the parameters in Table 4. It is important to note that C_D can only decrease as surface roughness increases.

To quantify the performance variation both cases are considered separately and modelled with the same procedure explained in Subsection 3.3, changing only C_D and injector diameter in their respective cases. Both occurrences are analyzed and reported in Subsection 4.2.

3.6 Shapiro's equations

Rocket nozzles undergo multiple simultaneous effects, including area variation, wall friction, shifts in molecular weight and specific heat due to combustion, evaporation and gas injection. Shapiro's equations predict the alterations in flow properties throughout the nozzle resulting from these diverse phenomena, but it is mainly indicated for the divergent. In the case analysed only the divergent part is considered and the equations used rely on the following assumptions:

- the flow is one-dimensional and steady;
- changes in stream properties are continuous;
- the gas is semi-perfect;
- neglect heat, work exchange and enthalpy terms;
- neglect drag forces.

The first three hypotheses are related to the general Shapiro's equations model, while the others are adapted to the case analysed. Referring to the total table of influence coefficients for variable specific heat and molecular weight [38], the system (can be seen in Appendix A 5, where also the independent and dependent variables considered are written) is solved thanks to its implementation in Matlab.

Considering the mass flow rate constant along the length of the divergent the further hypotheses $d\dot{m}/dx = 0$ is added.

The terms to perform the analysis are taken running CEAM for different expansion ratios, from 1 to 200, to simulate the increasing area profile, divergent length and properties change. In particular, γ_{GC} , $M_{mol,GC}$, $c_{p,GC}$, s_{GC} , ρ_{GC} and $T_{exit,GC}$. $a_{exit,GC}$ are directly derived from the mentioned analysis. The Darcy friction factor f is computed at each spatial discretization index thanks to the Moody diagram with mean roughness $\epsilon = 20 \mu m^2$, Reynolds number Re_{GC} and hydraulic diameter D (both the latter coming from CEAM run) at each step.

All this analysis is run at relevant time steps within the burning time t_b , such as the beginning, the end and two intermediate time steps.

The main results of this analysis are shown in the appropriate Section 4.3, while the complete results are present in Appendix A 5.

4 Results and comments

4.1 Nominal case

The results of the analysis regarding the most relevant quantities at the initial and final instants are shown in Table 15

	T [N]	P_c [bar]	O/F [-]	I_{sp} [s]	\dot{m}_p [kg/s]
Initial value	1000	50	2.352	353.856	0.2902
Final value	528.3	26.26	2.347	350.087	0.1550

Table 15: Initial and final values for relevant quantities

As it can be observed, the major requirements stated in Subsection 1.1 are successfully respected. As a matter of fact, both initial values for thrust and P_c and the final combustion pressure respect the constraints. The fact that the latter is much higher than the minimum allowable value states the capability of the system to face the possibility of working under the presence of uncertainties. It is worth to mention:

- **total impulse** $I_{tot} = 1610436 Ns^3$;
- **burning time** $t_b = 37 min$

²This roughness value is referred to surface roughness prediction for Inconel 718 by selective laser melting [27]

³Further discussed in the Conclusion5

All the values in the Table are reported just to complement the graphs and to guarantee a clearer understanding on the variations.

The results in time obtained for the nominal case, without considering any uncertainties due to AM, are shown in figure 11, 12, and 13.

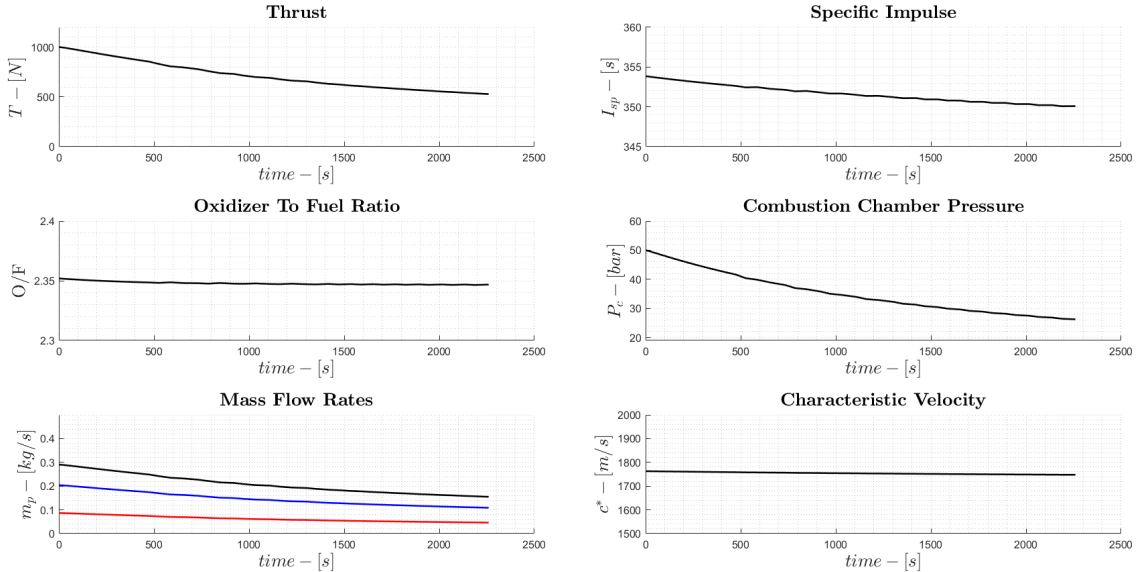


Figure 11: Variation of thrust, specific impulse, O/F with oxidizer (blue) and fuel (red), P_c , \dot{m} , and c^* versus time.

The thrust takes into account the 2D losses; in addition, its variation in time does not present any sudden changes, as expected during the sizing. Figure 11 shows how the thrust is almost halved at the end of the burn, as expected due to the reduced \dot{m}_p . The preliminary choice of a low blowdown ratio was made in order to achieve a gradual and smooth pressure reduction in the combustion chamber, so to avoid substantial drops of performances in time 3.2.6. The P_c graph in Figure 11 shows how this condition is indeed achieved since the obtained values do not change drastically nor suddenly. As for the combustion chamber, its pressure is more than half of the initial value at the end of the burn. Despite this, the final value is above the 20 bar set by requirement **REQ-03**.

Moreover, I_{sp} , c^* and O/F remain almost constant throughout the burn, and decrease only slightly, especially the last two. This is a positive fact, since it means that the engine, despite working in off-design conditions, is still maintaining a relatively constant efficiency. In particular, the slight decrease in the O/F ratio is beneficial as it indicates that the engine is prone to operate in a condition richer in fuel compared to its initial one. This is a common choice as fuel-rich mixtures are less prone to corrosion issues and result in a reduced temperature in the combustion chamber [21]. In addition to that, the fact that this change in O/F is minimal means that the temperature in the combustion chamber is almost constant too, explaining why c^* is approximately constant. The propellant flow rate has a smooth reduction, due to the necessity of a soft decrease of thrust; furthermore, it can be observed that the oxidizer and fuel mass flow rate have a similar behaviour, reflecting, therefore, on a small variation of O/F in time. It is noteworthy to draw attention to the mass expelled during the mission, the engine shuts off due to the full consumption of oxygen.

The final mass of *RP-1* remaining in the tank is about 0.5 kg. This value actually depends on the time discretization chosen during the time cycle: since the iteration process simulates the engine performance in small instants of time, the more the time step is small, the more is then possible to obtain a precise value of the unused propellant mass still stored in the tank, since the simulation would emulate better the real behaviour of the physical system. In this way, the iteration process will return a final value actually close to the real one.

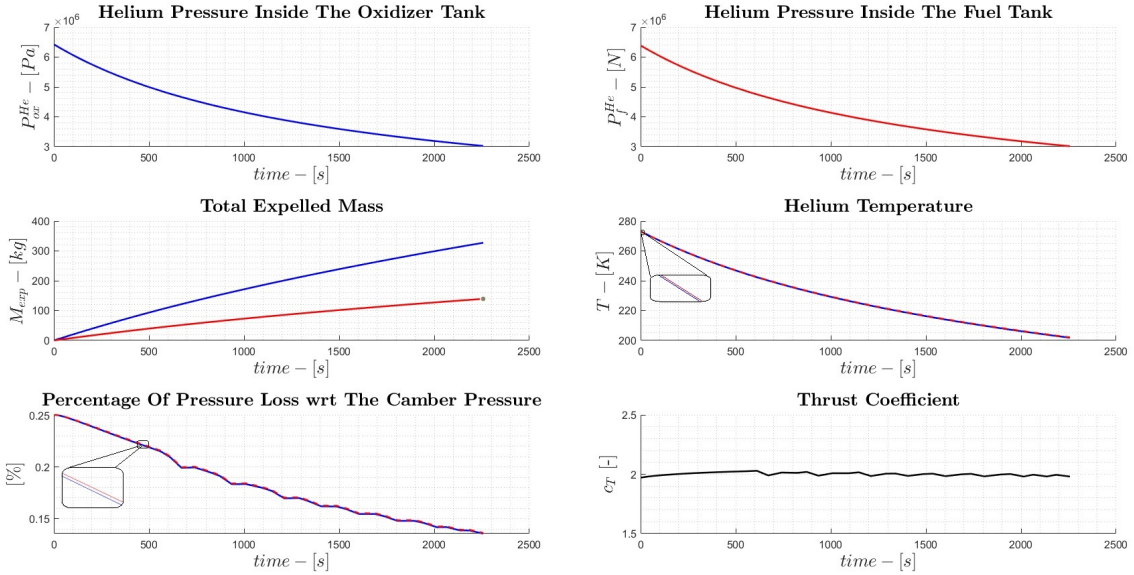


Figure 12: Variation of helium pressure in oxidizer (blue) and fuel (red) tanks, total expelled mass for both oxidizer and fuel, helium temperature for both tanks, percentage of pressure loss, and thrust coefficient versus time.

From the total expelled mass in Figure 12, by the end of the burn both LOX and RP-1 are completely expelled, meaning almost no residual propellant is left in the tanks, as such, the chosen tank design is utilizing fully the available space. Regarding c_T , its value increases slightly until oscillating asymptotically around the value of 2. This can be explained by the fact that, as time increases, the static contribution of thrust becomes less and less significant and, consequently, the contribution of the divergent part of the nozzle becomes more important. Since the temperature of pressuring gas is equal for both tanks (273.15K), its variation is the same for both tanks.

As shown in Figure 13, the exit pressure and the exit velocity decrease in time. Thus, these behaviours explain the trend of the thrust in time, which reduces too. The imposed condition of choked flow in the throat can be appreciated in Figure 13, where it is possible to observe that the Mach number at the throat oscillates around the value of 1. The Mach number in the combustion chamber is constant as well, oscillating around the value of 0.06. The reason why these quantities oscillate is due to the adopted discretization. Another interesting result is that the pressure drop trend of the injector is nearly equal for both LOX and RP-1, showing that both injectors are working to grant the combustion chamber pressure. O/F , as previously stated, slightly decreases due to the minor mismatch between the pressure drop at injection, for the two lines.

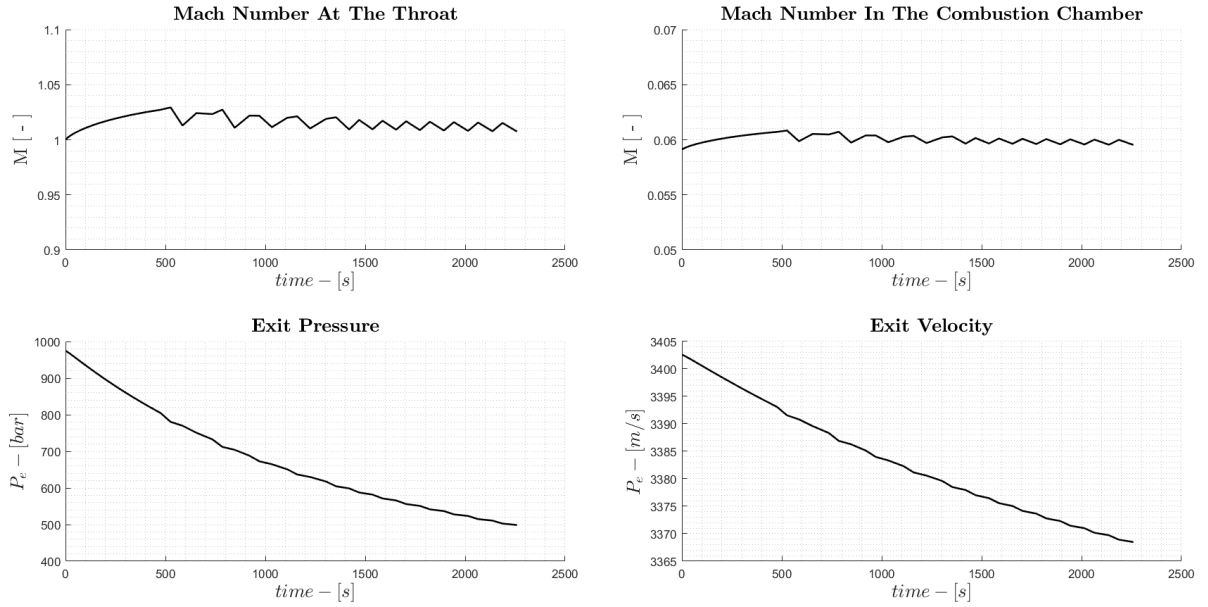


Figure 13: Variation of Mach number at throat, in combustion chamber, P_e and v_e versus time.

4.2 Additive manufacturing

Results obtained due to variation of both accuracy and roughness are reported in Figure 14.

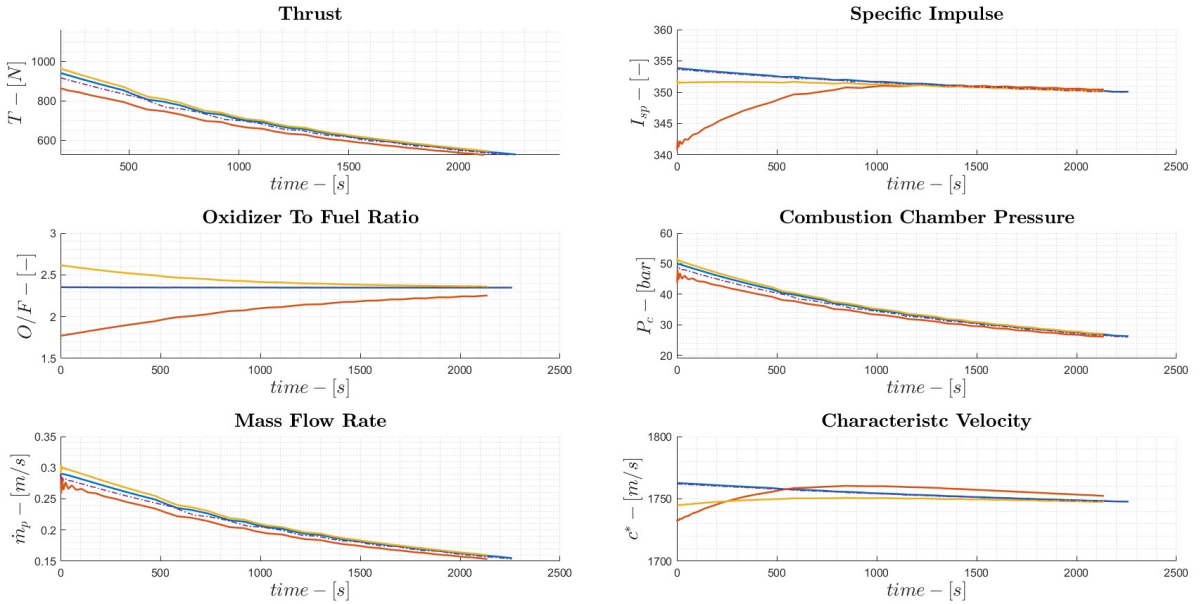


Figure 14: Variation due to AM. Blue: nominal case, red: lower bound of accuracy, yellow: upper bound of accuracy, dashed: variation due to C_D .

It is possible to notice that:

- **upper bound of uncertainty:** as expected, since the diameter of the injectors is overall larger compared to the nominal case, the total mass flow rate is higher and consequently a higher thrust compared to the nominal case is obtained and as such, the burning time is lower. I_{sp} is lower in this case since O/F is shifted away from the optimum;
- **lower bound of uncertainty:** in this case, CEAM with finite chamber is not capable of running its code for a diameter variation of $-60 \mu\text{m}$ so a variation of only $-40 \mu\text{m}$ is considered. This is supposed to

be a consequence of the very low O/F that is obtained in this situation and, as such, a finite chamber is not capable of achieving a successful combustion reaction. This can be achieved with an infinite combustion chamber, but such case is not considered in the analysis. Despite this, the overall behaviour of all parameters is acting as expected. A lower thrust is obtained due to a reduced \dot{m} . Specific impulse is also much lower mainly because the O/F ratio is lower than the optimum;

- **C_D variation due to roughness:** compared to uncertainties due to accuracy, variations of the discharge coefficient have a significantly lower impact. Despite this, variation due to a decreased C_D still produces relevant variations compared to the nominal case. In particular, the overall mass flow rate is reduced and, consequently, thrust is reduced. Compared to the first two cases, the O/F, I_{sp} , and c^* closely follow the nominal case. This shows that, between uncertainties due to resolution and the ones due to roughness, the latter is the least relevant one.

It can also be observed that both three cases have a tendency to reach the nominal one after the transient due to the initial conditions not being respected.

4.3 Shapiro's equations results

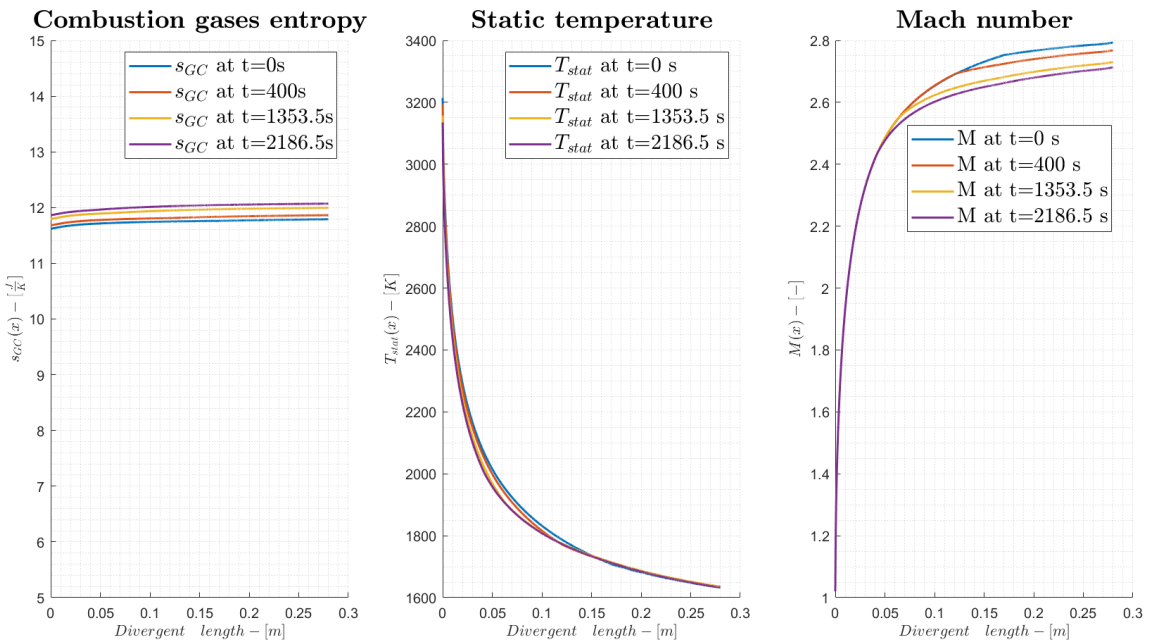


Figure 15: Combustion gases entropy (on the left), static temperature (at the center) and Mach number (on the right) along the divergent at different time steps

The plot on the left shows that entropy slightly increases along the divergent in all the instants analysed, this is due to the irreversible nature of the flow process and the dissipation of kinetic energy into the surroundings. This demonstrates that the assumptions of adiabatic nozzle are a good approximation of the real behaviour of the system.

The static temperature decreases along the divergent, as effects of the expansion. Consequently, the sonic velocity decreases (shown in 5).

Another result of the expansion in the nozzle is the fact that the Mach number increases along the divergent part, this, combined with the decrease of sonic velocity, implies that velocity of the flow increases (plot in 5), this has beneficial effects for the thrust generation. During the operational life (as time increases) Mach number M tends to decrease, meaning that the propulsion system is gradually less capable of maintaining the nominal design condition. This influences the decrease of the amount of thrust, dependent on the exit velocity (plot in 5), generated by the system. The behavior is typical of the blowdown architecture chosen for the mission.

5 Conclusion

To sum up, after a preliminary literature review, and accounting for the imposed requirements (1.1), the first assumptions were made. From these, the initial design was performed (3.2) and the model explained was developed (3) in order to observe the behaviour of the proposed engine fulfilling the requirements. Then the study was deepened checking the feasibility of the combustion chamber cooling (3.4), and proposing a possible alternative solution. Afterwards, the effects of different types of AM uncertainties were assessed (3.5). In the end, divergent physical quantities analysis was performed thanks to the implementation of Shapiro's equations. Overall, the designed system is capable of giving relatively high performances despite the tank pressurization architecture utilized. The high total impulse is linked more to the high burning time (*37 minutes*) rather than to the thrust, as previously hypothesized. This value may be comparable with the high-thrust apogee kick motor found in [30]. Such a long burn time could be justified in two ways: either this stage is employed as low-thrust propulsion, since the thrust provided is only 1 kN ; or the engine is going to be used for multiple burns. Considering the second case, an igniter that allows multiple ignitions would have to be employed, since the propellant couple LOX/RP-1 is not hypergolic.

From the observation of the mean value of the residence time $t_s = 1.685\text{ ms}$ (as shown in Appendix B 27), it can be noticed that it is quite low, maybe resulting in inefficient combustion, although being in the acceptable values range $< 10\text{ ms}$. The small value of t_s is an indication that the oxidizer and fuel combination chosen may be not suitable for the required thrust magnitude but, instead, would be more appropriate for higher thrust applications, such as first stages, as already described in Subsection 2.3. To obtain a higher value of residence time, the combustion chamber should be longer and narrower, option which would be unrealistic.

Further development can be related to pintle injectors, AM uncertainties estimation, and Computational Fluid Dynamics (CFD). Blowdown-fed engine can allow throttleability, using *pintle injectors* [36]. This additional design choice must be carefully weighted considering both advantages (such as throttling capability and simple design) and disadvantages (eventual combustion instability and risk of unburnt propellant) with respect to the constraints of a blowdown system [2].

Another design for the injection plate could also be studied to reduce the effects of AM uncertainties and avoid high-risk issues.

Regarding *AM uncertainties*, poor surface roughness does not constitute a significant issue, since it only affects the discharge coefficient of the injectors. Accuracy uncertainties, on the other hand, constitute a critical point which could completely lead the engine to failure for what concerns the case of injectors with a diameter of $40\text{ }\mu\text{m}$ smaller compared to the nominal case. In general, higher accuracy can be achieved but requires specific and more precise manufacturing techniques[28]. To further quantify the effects of such uncertainties, a more in-depth Monte Carlo simulation should be performed.

Note that one of the propellant is cryogenic, thus the risk of considerable boil-off of LOX needs to be taken into account. Consequently, significant thermal protection will have to be applied, both passive and active, if the system requires it.

To enhance the simulation and estimation of the flow trend and properties a *CFD* analysis can be run, which is far more precise than the fluid simulation performed.

References

- [1] GJ Adheena, Kalakanda Alfred Sunny, Aldin Justin, and Nallapaneni Manoj Kumar. “Effect of reynolds number and weber number on the estimation of droplet size for an injector”. In: *Technology* 9.3 (2018), pp. 382–391.
- [2] Erik Andersson. *Numerical Approach to the Design and Optimisation of a Bi-Propellant Pintle Injector*. 2022.
- [3] Tomasz Blachowicz, Guido Ehrmann, and Andrea Ehrmann. “Metal additive manufacturing for satellites and rockets”. In: *Applied Sciences* 11.24 (2021), p. 12036.
- [4] Byron Blakey-Milner, Paul Gradl, Glen Snedden, Michael Brooks, Jean Pitot, Elena Lopez, Martin Leary, Filippo Berto, and Anton du Plessis. “Metal additive manufacturing in aerospace: A review”. In: *Materials and Design* 209 (2021).
- [5] MATTIA BURINI. “Raccolta dati e analisi statistica della tensione superficiale di fluidi organici”. In: (2021).
- [6] XQ Cao, Robert Vassen, and Detler Stöver. “Ceramic materials for thermal barrier coatings”. In: *Journal of the European Ceramic Society* 24.1 (2004), pp. 1–10.
- [7] Bruce Chehroudi, Doug Talley, and Vigor Yang. “Liquid propellants and combustion: fundamentals and classifications”. In: *Encyclopedia of Aerospace Engineering* 2 (2010).
- [8] DATA SHEET ALLOY 718 | 2.4668. <https://www.sd-metals.com/it/materiali-s-d/leghe-di-nichel-e-cobalto/alloy-718-2-4668/>.
- [9] T. DebRoy, H.L. Wei, J.S. Zuback, T. Mukherjee, J.W. Elmer, J.O. Milewski, A.M. Beese, A. Wilson-Heid, A. De, and W. Zhang. “Additive manufacturing of metallic components – Process, structure and properties”. In: *Progress in Materials Science* 92 (2018), pp. 112–224.
- [10] T Dharini, P Kuppusami, A M Kamalan Kirubaharan, R Ramaseshan, Arul Maximus Rabel, and S Dash. “Influence of substrate temperature on the adhesion property of YSZ coatings on inconel 718 prepared by EBPVD”. In: *Advanced Materials Letters* 7.10 (2016), pp. 826–830.
- [11] EV Dudnik, SN Lakiza, IN Hrechanyuk, AK Ruban, VP Redko, IO Marek, VB Shmibelsky, AA Makudera, and NI Hrechanyuk. “Thermal barrier coatings based on ZrO₂ solid solutions”. In: *Powder Metallurgy and Metal Ceramics* 59 (2020), pp. 179–200.
- [12] Tim Edwards. “Liquid Fuels and Propellants for Aerospace Propulsion: 1903–2003”. In: *Journal of Propulsion and Power* 19.6 (November–December 2003).
- [13] Nicholas Gloria, Wade Bassett, Ian Vorbach, James Kolano, Akshay Gupta, Alexander Kaplan, Ian Rall, Nicholas Folz, and Shane Dirks. “Performance of a Small-Orifice Rocket Injector Utilizing Additive Manufacturing”. In: *Proceedings of AIAA Propulsion and Energy Forum*. Indianapolis, IN, 19-22 August 2019.
- [14] Sanford Gordon and Bonnie J McBride. “Computer Program for Calculation of Complex Chemical Equilibrium Compositions and Applications (NASA Reference Publication 1311; Cleveland, OH: NASA)”. In: *Cleveland, Ohio, USA* (1994).
- [15] Paul Gradl, Sandy E. Greene, Christopher Protz, Brad Bullard, James Buzzell, Chance Garcia, Jessica Wood, Kenneth Cooper, James Hulka, and Robin Osborne. “Additive Manufacturing of Liquid Rocket Engine Combustion Devices: A Summary of Process Developments and Hot-Fire Testing Results”. In: *Proceedings of 54th AIAA Propulsion and Energy Forum*. 2018 Joint Propulsion Conference. Cincinnati, Ohio, July 9-11, 2018.
- [16] Don W. Green and Robert H. Perry. *Perry's Chemical Engineers' Handbook*. 7th. McGraw-Hill Education, December 1st, 2007.
- [17] John A. Halchak, James L. Cannon, and Corey D. Brown. *Materials for liquid propulsion systems*. Jan. 2018, pp. 641–698. DOI: 10.2514/5.9781624104893.0641.0698. URL: <https://doi.org/10.2514/5.9781624104893.0641.0698>.

- [18] Howard JM Hanley, Robert D McCarty, and JV Sengers. *Viscosity and thermal conductivity coefficients of gaseous and liquid oxygen*. Tech. rep. NASA, 1974.
- [19] Philip D. Harvey. *Engineering Properties of Steels*. American Society for Metals, Metals Park, OH, (1982).
- [20] Ronald W. Humble, Gary N. Henry, and Wiley J. Larson. *Space Propulsion Analysis And Design*. The McGraw-Hill Companies, Inc., 1995.
- [21] Dieter K. Huzel and David H. Huang. “Design of liquid propellant rocket engines. NASA SP-125”. In: *NASA Special Publication 125* (Jan. 1971). URL: <https://ui.adsabs.harvard.edu/abs/1971NASSP.125....H/abstract>.
- [22] Qingbo Jia and Dongdong Gu. “Selective laser melting additive manufacturing of Inconel 718 superalloy parts: Densification, microstructure and properties”. In: *Journal of Alloys and Compounds* 585 (2014), pp. 713–721.
- [23] Benjamin P Keller, Shawn E Nelson, Kyle L Walton, Tushar K Ghosh, Robert V Tompson, and Sudarshan K Loyalka. “Total hemispherical emissivity of Inconel 718”. In: *Nuclear Engineering and Design* 287 (2015), pp. 11–18.
- [24] Fabio Kerstens, Angelo Cervone, and Paul Gradl. “End to end process evaluation for additively manufactured liquid rocket engine thrust chambers”. In: *Acta Astronautica* 182 (2021), pp. 454–465.
- [25] *Latch valves*. <https://www.valcor.com/missiles-and-aerospace/aerospace-latch-valves/>.
- [26] T.W. Lau and N.R. Afshar. “Effect of Roughness on Discharge”. In: *UNIMAS e-Journal of Civil Engineering* 4 (3 December 2013).
- [27] Cuiyuan Lu and Jing Shi. “Relative density and surface roughness prediction for Inconel 718 by selective laser melting: central composite design and multi-objective optimization”. In: *The International Journal of Advanced Manufacturing Technology/International Journal, Advanced Manufacturing Technology* 119.5-6 (Jan. 2022), pp. 3931–3949. DOI: 10.1007/s00170-021-08388-2. URL: <https://doi.org/10.1007/s00170-021-08388-2>.
- [28] Xact metals. *Best practices for metal powered-bed fusion additive manufacturing*. Design guide.
- [29] USAF Michael C. Waters B.S.A.E. 2d Lt. “Analysis of additively manufactured injectors for rotating detonation engines”. PhD thesis. Department of the air force, air university, air force institute of technology, Wright-Patterson Air Force Base, Ohio, March 8, 2018.
- [30] Nolan Naicker, Ronan Wall, and David Perigo. “An overview of development model testing for the LEROS 4 High Thrust Apogee Engine”. In: *2014 Space Propulsion Conference*. Vol. 2969298. 2014.
- [31] *NIST Chemistry WebBook*. <https://webbook.nist.gov/chemistry/>.
- [32] *NSS 1740.15: Safety Standards for Oxygen and Oxygen Systems: Guidelines for Oxygen System Design, Materials Selection, Operations, Storage, and Transportation*. Standard. National Aeronautics and Space Administration, January, 1995.
- [33] Stephanie L Outcalt, Arno Laesecke, and Karin J Brumback. “Thermophysical properties measurements of rocket propellants RP-1 and RP-2”. In: *Journal of Propulsion and Power* 25.5 (2009), pp. 1032–1040.
- [34] Maurizio Quadrio. “Flussi comprimibili”. In: (2003). URL: <https://home.aero.polimi.it/quadrio/it/Didattica/2003/cap09.pdf>.
- [35] Maurizio Quadrio. “Forme alternative delle equazioni”. In: (2003). URL: <https://home.aero.polimi.it/quadrio/it/Didattica/2003/cap02.pdf>.
- [36] R Rajendran, Samiksha Prasad, S Subhashree, Toshith S Phutane, and Vedanth S Saoor. “Design and optimization of pintle injector for liquid rocket engine”. In: *Int. J. Eng. Appl. Sci. Technol* 5 (2020), pp. 151–159.
- [37] Richard Roback, EJ Szetela, and Louis J Spadaccini. *Deposit formation in hydrocarbon rocket fuels*. Tech. rep. 1981.
- [38] Ascher H. Shapiro. *Dynamics and thermodynamics of compressible fluid flow*. Jan. 1953.

- [39] S. Soller, S. Beyer, A. Dahlhaus, A. Konrad, J. Kretschmer, N. Rackemann, and W. Zeiss. “Development of Liquid Rocket Engine Injectors Using Additive Manufacturing”. In: *Proceedings of the 6th European Conference for Aerospace Sciences*. EUCASS. 2015.
- [40] United States Military Standard. *MIL-DTL-25576E, Detail Specification: Propellant, Rocket-Grade Kerosene*. Specification. April 14th, 2006.
- [41] George P. Sutton and Oscar Biblarz. *Rocket Propulsion Elements*. John Wiley and Sons, Inc., Hoboken, New Jersey, 2017.
- [42] Yang Tan, Vasudevan Srinivasan, Toshio Nakamura, Sanjay Sampath, Pierre Bertrand, and Ghislaine Bertrand. “Optimizing compliance and thermal conductivity of plasma sprayed thermal barrier coatings via controlled powders and processing strategies”. In: *Journal of thermal spray technology* 21 (2012), pp. 950–962.
- [43] Shiqian Tao, Jianli Yang, Minglong Zhai, Fang Shao, Xinghua Zhong, Hao Zhao, Yin Zhuang, Jie Ni, Wei Li, and Shunyan Tao. “Thermal stability of YSZ thick thermal barrier coatings deposited by suspension and atmospheric plasma spraying”. In: *Crystals* 10.11 (Oct. 2020), p. 984. DOI: 10 . 3390 / cryst10110984. URL: <https://doi.org/10.3390/cryst10110984>.
- [44] Gokturk Tunc, Howard Wagner, and Yildiz Bayazitoglu. “Space shuttle upgrade liquid oxygen tank thermal stratification”. In: *35th AIAA Thermo physics Conference*. 2001, p. 3082.
- [45] Ching Kiat Yong, Gregory J Gibbons, Chow Cher Wong, and Geoff West. “A critical review of the material characteristics of additive manufactured IN718 for high-temperature application”. In: *Metals* 10.12 (2020), p. 1576.
- [46] *Yttria-stabilized Zirconia Ceramic Performance Parameters*. <https://great-ceramic.com/zirconia-ceramics/>.
- [47] Yi Zhang and Jing Zhang. “First principles study of structural and thermodynamic properties of zirconia”. In: *Materials Today: Proceedings* 1.1 (2014), pp. 44–54.

Appendix A

Performance

The following is the system of equations used to find A_e , A_T and \dot{m}_p :

$$\begin{cases} T = \dot{m}_p v_e + A_e P_e \\ A_e = \epsilon A_t \\ C_{id}^* = \frac{P_e A_t}{\dot{m}_p} = C_{exp}^* \end{cases} \quad (25)$$

Tank Sizing

$$t_{tank} = \frac{P_{tank} r_{tank}}{\sigma} \quad (26)$$

$$m_{tank} = \rho \cdot h_{tank} \left(\pi (r_{tank} + t_{tank})^2 - \pi \cdot r_{tank}^2 \right) \quad (27)$$

Where r_{tank} is the radius of the tanks (0.5 m) and h_{tank} is the height.

Blowdown cycle

The complete system solved through Matlab for the blowdown system and its unknowns are:

$$\left\{ \begin{array}{l} M_{esp,OX}(i-1) = \dot{m}_{OX}(i)dt \\ M_{esp,F}(i-1) = \dot{m}_F(i)dt \\ V_{esp,OX}(i-1) = \frac{M_{esp,OX}(i-1)}{\rho_{OX}} \\ V_{esp,F}(i-1) = \frac{M_{esp,F}(i-1)}{\rho_F} \\ V_{He,OX}(i) = V_{He,OX}(i-1) + V_{esp,OX}(i-1) \\ V_{He,F}(i) = V_{He,F}(i-1) + V_{esp,F}(i-1) \\ V_{OX}(i) = V_{OX}(i-1) - V_{esp,OX}(i-1) \\ V_F(i) = V_F(i-1) - V_{esp,F}(i-1) \\ T_{He,OX}(i-1)V_{He,OX}(i-1)^{(\gamma_{He}-1)} = T_{He,OX}(i)V_{He,OX}(i)^{\gamma_{He}-1} \\ P_{He,OX}(i)V_{He,OX}(i) = M_{He,OX} \frac{R}{Mm_{He}} T_{He,OX}(i) \\ T_{He,F}(i-1)V_{He,F}(i-1)^{\gamma_{He}-1} = T_{He,F}(i)V_{He,F}(i)^{\gamma_{He}-1} \\ P_{He,F}(i)V_{He,F}(i) = M_{He,F} \frac{R}{Mm_{He}} T_{He,F}(i) \\ u_{OX}(i) = \frac{\dot{m}_{OX}(i)}{\rho_{OX} A_{OX}^{pipe}} \\ u_F(i) = \frac{\dot{m}_F(i)}{\rho_F A_F^{pipe}} \\ P_{He,OX}(i) = P_{c,OX}(i) + \frac{1}{2} \rho_{OX} u_{OX}(i)^2 + \Delta P_{feed} + x(i) P_{c,OX}(i) \\ P_{He,F}(i) = P_{c,F}(i) + \frac{1}{2} \rho_F u_F(i)^2 + \Delta P_{feed} + x(i) P_{c,F}(i) \\ P_{c,OX}(i) = P_{c,F}(i) \\ \dot{m}_{OX}(i) = C_{D,OX} A_{OX}^{inj} \sqrt{2 \rho_{OX} x(i) P_{c,OX}(i)} \\ \dot{m}_F(i) = C_{D,F} A_F^{inj} \sqrt{2 \rho_F y(i) P_{c,F}(i)} \\ \dot{m}_p(i) = \dot{m}_{OX}(i) + \dot{m}_F(i) \\ M_t(i) = \frac{\frac{\dot{m}_p(i)}{\rho_{GC,t}(i-1) A_t}}{\sqrt{\gamma_{GC}(i-1) \frac{R}{Mm_{GC}(i-1)} T_{GC}(i-1)}} \end{array} \right. \rightarrow \left\{ \begin{array}{l} M_{esp,OX}(i-1) \\ M_{esp,F}(i-1) \\ V_{esp,OX}(i-1) \\ V_{esp,F}(i-1) \\ V_{He,OX}(i) \\ V_{He,F}(i) \\ V_{OX}(i) \\ V_F(i) \\ \dot{m}_{OX}(i) \\ \dot{m}_F(i) \\ \dot{m}_p(i) \\ T_{He,OX}(i) \\ P_{He,OX}(i) \\ T_{He,F}(i) \\ P_{He,F}(i) \\ x(i) \\ y(i) \\ P_{c,OX}(i) \\ P_{c,F}(i) \\ u_{OX}(i) \\ u_F(i) \end{array} \right. \quad (28)$$

Shapiro Equations

The table where the subsequent equations were taken is:

TABLE 8.1
INFLUENCE COEFFICIENTS FOR VARIABLE SPECIFIC HEAT AND MOLECULAR WEIGHT

	$\frac{dA}{A}$	$\frac{dQ - dW_x + dH}{c_p T}$	$4f \frac{dx}{D} + \frac{dX}{\frac{1}{2} kp A M^2} - 2y \frac{dw}{w}$	$\frac{dw}{w}$	$\frac{dW}{W}$	$\frac{dk}{k}$
$\frac{dM^2}{M^2}$	$\frac{2 \left(1 + \frac{k-1}{2} M^2\right)}{1 - M^2}$	$\frac{1 + kM^2}{1 - M^2}$	$\frac{kM^2 \left(1 + \frac{k-1}{2} M^2\right)}{1 - M^2}$	$\frac{2(1 + kM^2) \left(1 + \frac{k-1}{2} M^2\right)}{1 - M^2}$	$\frac{1 + kM^2}{1 - M^2}$	-1
$\frac{dV}{V}$	$\frac{1}{1 - M^2}$	$\frac{1}{1 - M^2}$	$\frac{kM^2}{2(1 - M^2)}$	$\frac{1 + kM^2}{1 - M^2}$	$\frac{1}{1 - M^2}$	0
$\frac{dc}{c}$	$\frac{k-1}{2} M^2$	$\frac{1 - kM^2}{2(1 - M^2)}$	$-\frac{k(k-1)M^4}{4(1 - M^2)}$	$-\frac{k-1}{2} M^2 (1 + kM^2)$	$\frac{kM^2 - 1}{2(1 - M^2)}$	$\frac{1}{2}$
$\frac{dT}{T}$	$\frac{(k-1)M^2}{1 - M^2}$	$\frac{1 - kM^2}{1 - M^2}$	$-\frac{k(k-1)M^4}{2(1 - M^2)}$	$-\frac{(k-1)M^2(1 + kM^2)}{1 - M^2}$	$\frac{(k-1)M^2}{1 - M^2}$	0
$\frac{dp}{p}$	$\frac{M^2}{1 - M^2}$	$-\frac{1}{1 - M^2}$	$-\frac{kM^2}{2(1 - M^2)}$	$-\frac{(k+1)M^2}{1 - M^2}$	$\frac{1}{1 - M^2}$	0
$\frac{dp}{p}$	$\frac{kM^2}{1 - M^2}$	$-\frac{kM^2}{1 - M^2}$	$-\frac{kM^2[1 + (k-1)M^2]}{2(1 - M^2)}$	$-\frac{2kM^2 \left(1 + \frac{k-1}{2} M^2\right)}{1 - M^2}$	$\frac{kM^2}{1 - M^2}$	0
$\frac{dF}{F}$	$\frac{1}{1 + kM^2}$	0	$-\frac{kM^2}{2(1 + kM^2)}$	0	0	0
$\frac{ds/c_p}{(Note 2)}$	0	1	$\frac{(k-1)M^2}{2}$	$(k-1)M^2$	0	0

Notes: (1) Each influence coefficient represents the partial derivative of the variable in the left-hand column with respect to the variable in the top row; for example

$$\cdot \frac{dM^2}{M^2} = -\frac{2 \left(1 + \frac{k-1}{2} M^2\right)}{1 - M^2} \frac{dA}{A} + \frac{1 + kM^2}{1 - M^2} \frac{dQ - dW_x + dH}{c_p T} + \dots - \frac{dk}{k}$$

(2) For unaltered chemical composition only, and referring to entropy change of main stream. See Eq. 8.26 for total entropy change.

Figure 16: Influence Coefficients for Variables Specific Heat and Molecular Weight

The system solved in Matlab is:

$$\begin{cases} \frac{dM^2}{dx} = \left(\frac{\gamma M^2 (1 + \frac{\gamma-1}{2} M^2)}{1 - M^2} \frac{4C_f}{D} - 2 \frac{(1 + \frac{\gamma-1}{2} M^2)}{1 - M^2} \frac{dA}{dx} \frac{1}{A} + 2 \frac{(1 + \gamma M^2)(1 + \frac{\gamma-1}{2} M^2)}{1 - M^2} \frac{d\dot{m}}{dx} \frac{1}{\dot{m}} - \frac{1 + \gamma M^2}{1 - M^2} \frac{dM_{mol}}{dx} \frac{1}{M_{mol}} - \frac{1}{\gamma} \frac{d\gamma}{dx} \right) M^2; \\ \frac{da}{dx} = \left(\frac{(\gamma-1)M^2}{1 - M^2} \frac{dA}{dx} \frac{1}{A} - \frac{\gamma(\gamma-1)M^2}{4(1 - M^2)} \frac{4C_f}{D} - \frac{(\frac{\gamma-1}{2} M^2(1 + \gamma M^2))}{1 - M^2} \frac{d\dot{m}}{dx} \frac{1}{\dot{m}} + \frac{\gamma M^2 - 1}{2(1 - M^2)} \frac{dM_{mol}}{dx} \frac{1}{M_{mol}} + \frac{1}{2} \frac{1}{\gamma} \frac{d\gamma}{dx} \right) a; \\ \frac{dT}{dx} = \left(\frac{(\gamma-1)M^2}{1 - M^2} \frac{dA}{dx} \frac{1}{A} - \frac{\gamma(\gamma-1)M^2}{2(1 - M^2)} \frac{4C_f}{D} - \frac{(\gamma-1)M^2(1 + \gamma M^2)}{1 - M^2} \frac{d\dot{m}}{dx} \frac{1}{\dot{m}} + \frac{(\gamma-1)M^2}{1 - M^2} \frac{dM_{mol}}{dx} \frac{1}{M_{mol}} \right) T; \\ \frac{d\rho}{dx} = \left(-\frac{\gamma M^2}{2(1 - M^2)} \frac{4C_f}{D} + \frac{M^2}{1 - M^2} \frac{dA}{dx} \frac{1}{A} - \frac{(\gamma+1)M^2}{1 - M^2} \frac{d\dot{m}}{dx} \frac{1}{\dot{m}} + \frac{1}{1 - M^2} \frac{dM_{mol}}{dx} \frac{1}{M_{mol}} \right) \rho; \\ \frac{dp}{dx} = \left(-\frac{\gamma M^2(1 + (\gamma-1)M^2)}{2(1 - M^2)} \frac{4C_f}{D} + \frac{\gamma M^2}{1 - M^2} \frac{dA}{dx} \frac{1}{A} - \frac{2\gamma M^2(1 + \frac{\gamma-1}{2} M^2)}{1 - M^2} \frac{d\dot{m}}{dx} \frac{1}{\dot{m}} + \frac{\gamma M^2}{1 - M^2} \frac{dM_{mol}}{dx} \frac{1}{M_{mol}} \right) p; \\ \frac{ds}{dx} = \left(\frac{(\gamma-1)M^2}{2} \frac{4f}{D} + (\gamma-1)M^2 \frac{d\dot{m}}{dx} \frac{1}{\dot{m}} \right) c_p \end{cases}$$

The independent variables used are:

$$\left\{ \frac{dA}{A}, \quad 4f \frac{dx}{D}, \quad \frac{\dot{m}}{\dot{m}}, \quad \frac{M_{mol}}{M_{mol}}, \quad \frac{d\gamma}{\gamma} \right\}^T \quad (29)$$

The dependent variables used are:

$$\left\{ \frac{dM^2}{M^2}, \quad \frac{da}{a}, \quad \frac{dT}{T}, \quad \frac{d\rho}{\rho}, \quad \frac{dp}{p}, \quad \frac{ds}{c_p} \right\}^T \quad (30)$$

Shapiro's Equations plots

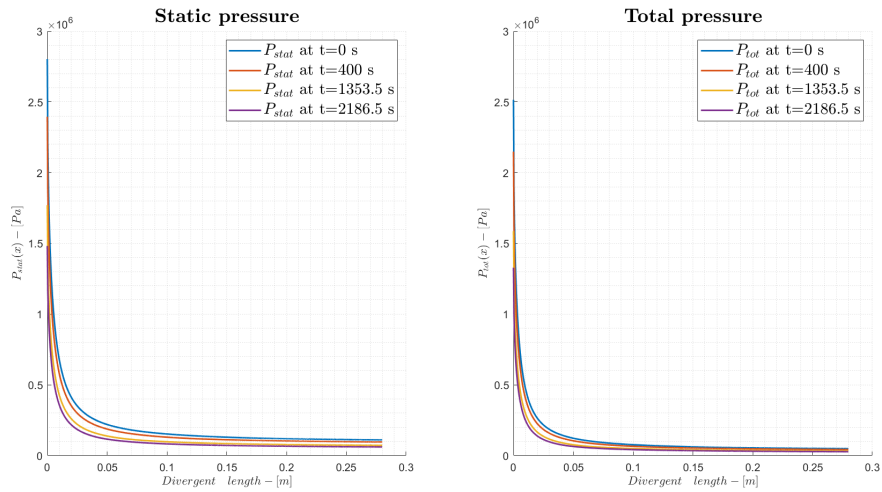


Figure 17: Static and total pressure plots along the divergent for different time instants

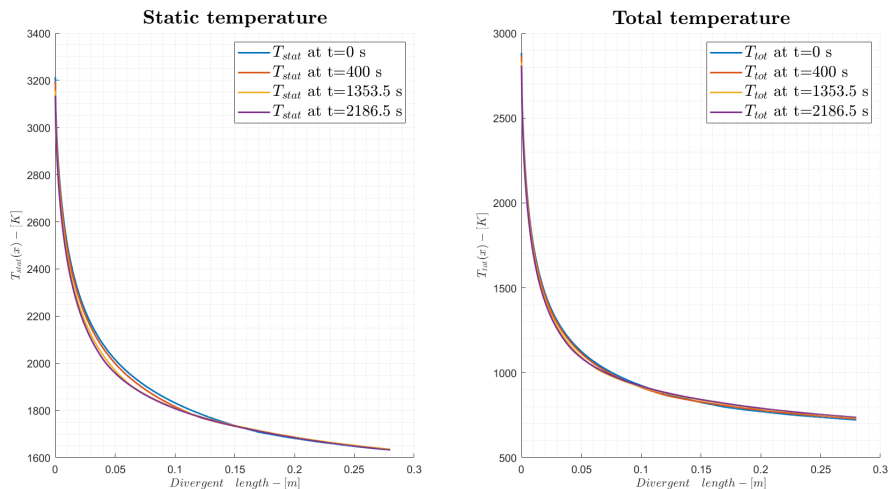


Figure 18: Static and total temperature plots along the divergent for different time instants

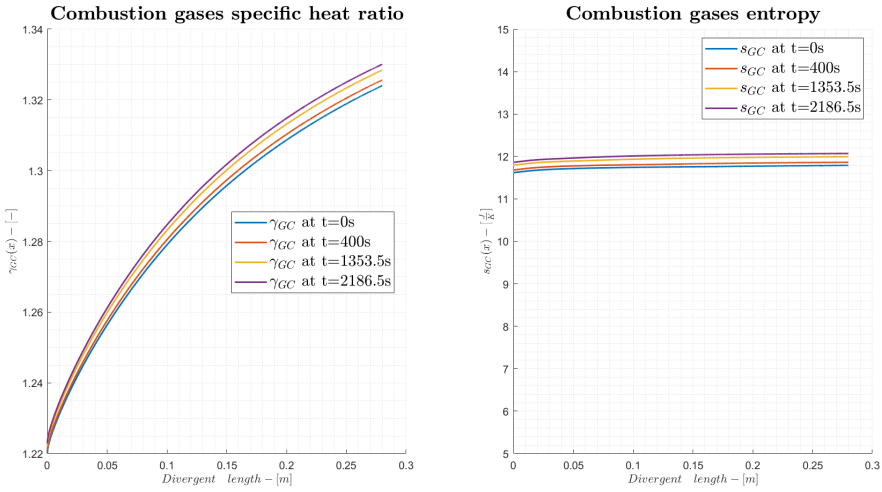


Figure 19: Combustion gases specific heat and entropy plots along the divergent for different time instants

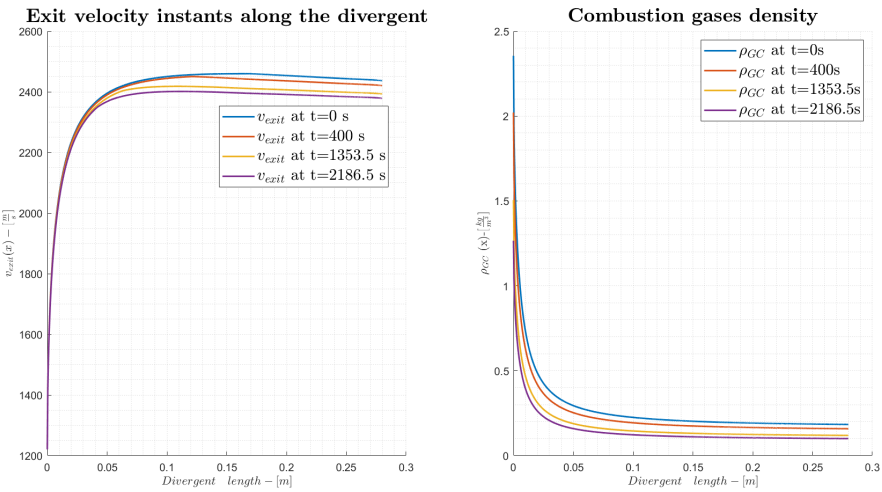


Figure 20: Exit velocity and combustion gases density plots along the divergent for different time instants

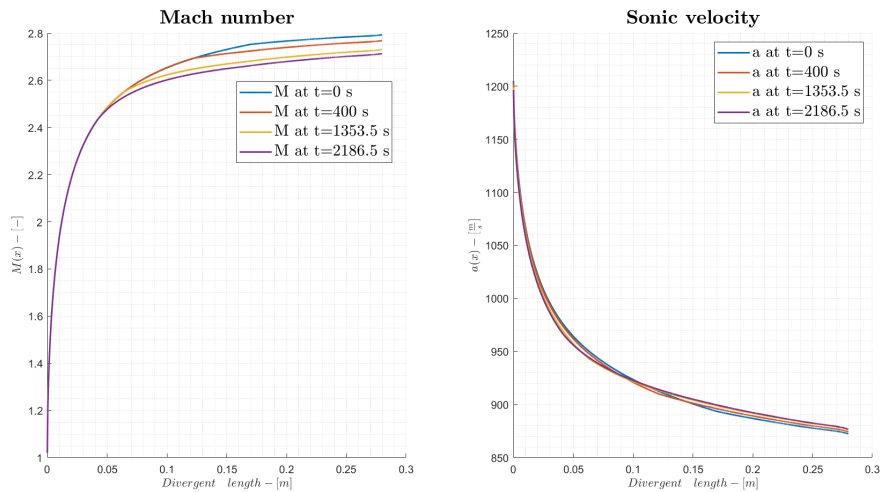


Figure 21: Mach and sonic velocities plots along the divergent for different time instants

Iterative system -Initial Volume and Mass estimation

$$\begin{cases} B_{ox} = \left(\frac{V_{f,He,Ox}}{V_{in,He,Ox}}\right)^\gamma \\ B_f = \left(\frac{V_{f,He,fu}}{V_{in,He,fu}}\right)^\gamma \\ T_{in,He,ox} V_{in,He,ox}^{\gamma-1} = T_{f,He,ox} V_{f,He,ox}^{\gamma-1} \\ T_{in,He,fuel} V_{in,He,fuel}^{\gamma-1} = T_{f,He,fuel} V_{f,He,fuel}^{\gamma-1} \\ V_{f,He,Ox} = V_{f,He,fu} \cdot K \\ V_{available} = V_{f,He,Ox} + V_{f,He,fu} \end{cases}$$

Note 1: $V_{available} = 0.8 \cdot V_{tot} - V_c$, represents the volume available for the two tanks.

Note 2: $K = \frac{V_{f,He,Ox}}{V_{f,He,fu}}$

Iterative system - volume ratio

$$\begin{cases} B_{ox} V_{in,He,Ox}^\gamma - V_{f,He,Ox}^\gamma \\ T_{in,He,Ox} V_{in,He,Ox}^{\gamma-1} - T_{f,He,Ox} V_{f,He,Ox}^{\gamma-1} \\ B_{fuel} V_{in,He,fuel}^\gamma - V_{f,He,fuel}^\gamma \\ T_{in,He,fuel} V_{in,He,fuel}^{\gamma-1} - T_{f,He,fuel} V_{f,He,fuel}^{\gamma-1} \\ V_{f,He,Ox} - V_{f,He,fuel} \cdot r \\ V_{f,He,Ox} - V_{f,He,fuel} - V_{tanks} \end{cases}$$

Note: $V_{tank} = V_{available} \cdot 0.8 - V_{cc}$, where $V_{available}$ is defined as the value with the dimension given by the problem and γ is the one of the helium. The r is defined as the the ratio of the volume $\frac{V_{ox}}{V_{fuel}}$

Appendix B

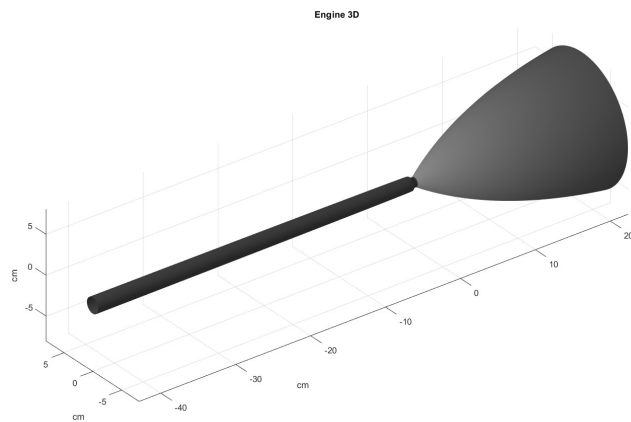


Figure 22: Alternative design of combustion chamber, fixing $M_c = 0.2$

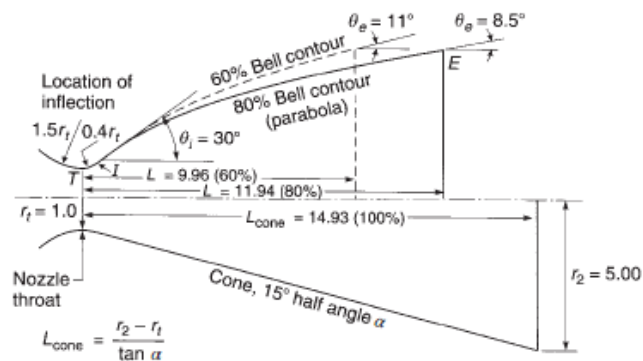


Figure 23: Rao nozzle [41]

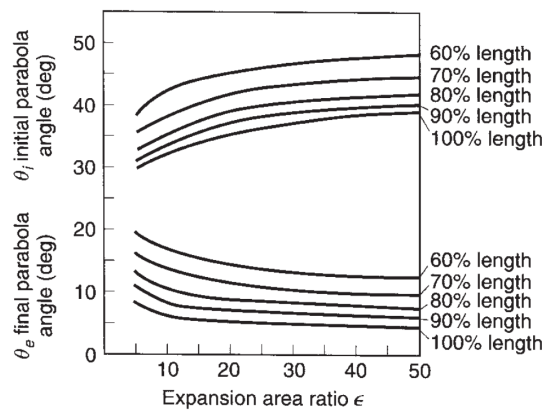


Figure 24: Initial and final parabola angles for Rao nozzle [41].

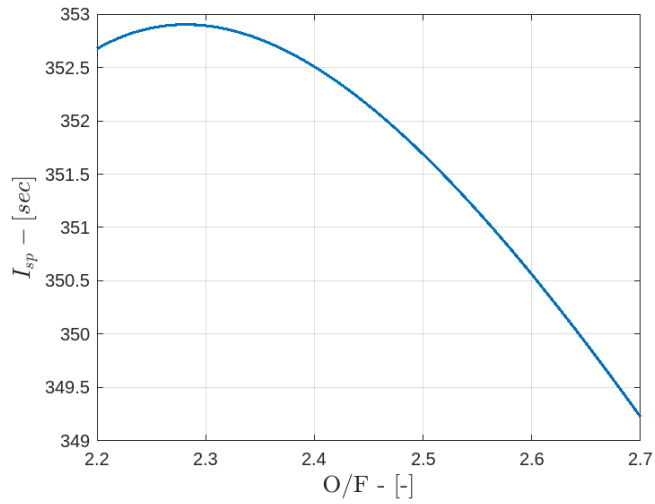


Figure 25: Vacuum Specific Impulse Versus Mixture Ratio for LOX and RP-1 Computed for 50 bar of Chamber Pressure

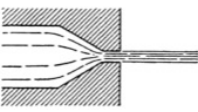
Orifice Type	Diagram	Diameter (mm)	Discharge Coefficient
Short tube with conical entrance		0.50	0.7
		1.00	0.82
		1.57	0.76
		2.54	0.84–0.80
		3.18	0.84–0.78

Figure 26: Type of injector chosen [41]

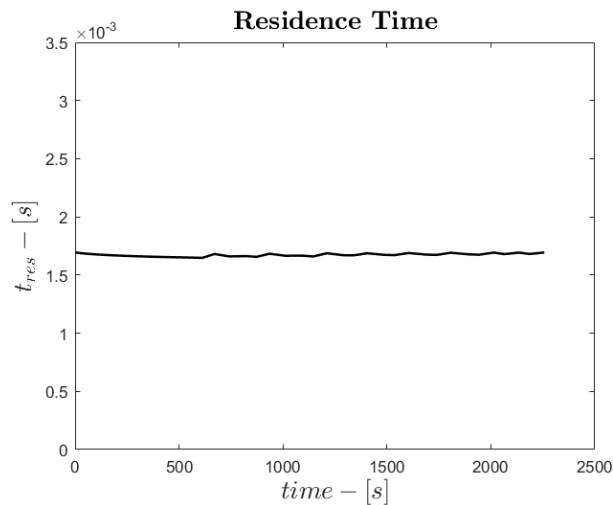


Figure 27: residence time during the mission

Declaration of Authorship

- Yijing Huang: atomization literature review and design; injection plate literature review and design; cooling literature review and design; conceptual contribute to initial sizing and blowdown model.
- Cristian Mandolini: AM literature review and modelling, tank literature review and sizing, nozzle design, conceptual contribute to initial sizing iteration and blowdown model development.
- Maurizio Ondeggia: injection plate literature review and design, AM literature review and modelling, conceptual contribute to initial sizing iteration and blowdown model development
- Francesco Gardiol: valves literature review; feeding architecture and pressure drop literature review; initial sizing; nozzle literature review and modelling; blowdown system literature review, modelling and programming.
- Chiara Conte: Literature review on material, literature review on the cooling strategy and implementation, conceptual contribute to initial sizing iteration and blowdown model development.
- Elisa Fiume : literature review on liquid propellant, literature review on the cooling strategy and implementation, conceptual contribute to initial sizing iteration and blowdown model development.
- Martina Angela Vurro: atomization literature review and modelling, injection plate literature review and design, cooling literature review and implementation, conceptual contribute to initial sizing and blowdown model development.
- Emanuele Gallo: Nozzles literature review, sizing and coding; conceptual contribute to initial sizing (pressure drop); Blowdown architecture and cycle literature review, sizing and coding; CEAM; Shapiro's equations conceptual development and coding.
- Adam Lakrad: Nozzles literature review, sizing and coding; Blowdown cycle literature review, sizing and coding; injectors coding; feeding architecture and pressure drop literature review, sizing and coding; Additive manufacturing coding; CEAM.